

A SYSTEMATIC TMRT OBSERVATIONAL STUDY OF GALACTIC $^{12}\text{C}/^{13}\text{C}$ RATIOS FROM FORMALDEHYDE

Y. T. YAN,¹ J. S. ZHANG,¹ C. HENKEL,^{2,3} T. MUFAKHAROV,^{4,5} L. W. JIA,¹ X. D. TANG,^{2,6,7} Y. J. WU,^{4,7} J. LI,^{4,7}
Z. A. ZENG,¹ Y. X. WANG,¹ Y. Q. LI,¹ J. HUANG,¹ AND J. M. JIAN¹

¹*Center for Astrophysics, Guangzhou University, 510006 Guangzhou, PR China*

²*Max-Planck-Institut für Radioastronomie, Auf dem Hügel 69, 53121 Bonn, Germany*

³*Astronomy Department, King Abdulaziz University, P.O. Box 80203, 21589 Jeddah, Saudi Arabia*

⁴*Shanghai Astronomical Observatory, Chinese Academy of Sciences, 200030 Shanghai, PR China*

⁵*Kazan Federal University, 18 Kremlyovskaya St., 420008 Kazan, Russia*

⁶*Xinjiang Astronomical Observatory, Chinese Academy of Sciences, 830011 Urumqi, PR China*

⁷*Key Laboratory of Radio Astronomy, Chinese Academy of Sciences, PR China*

(Received XXX; Revised YYY; Accepted ZZZ)

Submitted to ApJ

ABSTRACT

We present observations of the C-band $1_{10} - 1_{11}$ (4.8 GHz) and Ku-band $2_{11} - 2_{12}$ (14.5 GHz) K-doublet lines of H_2CO and the C-band $1_{10} - 1_{11}$ (4.6 GHz) line of H_2^{13}CO toward a large sample of Galactic molecular clouds, through the Shanghai Tianma 65-m radio telescope (TMRT). Our sample with 112 sources includes strong H_2CO sources from the TMRT molecular line survey at C-band and other known H_2CO sources. All three lines are detected toward 38 objects (43 radial velocity components) yielding a detection rate of 34%. Complementary observations of their continuum emission at both C- and Ku-bands were performed. Combining spectral line parameters and continuum data, we calculate the column densities, the optical depths and the isotope ratio $\text{H}_2^{12}\text{CO}/\text{H}_2^{13}\text{CO}$ for each source. To evaluate photon trapping caused by sometimes significant opacities in the main isotopologue's rotational mm-wave lines connecting our measured K-doublets, and to obtain $^{12}\text{C}/^{13}\text{C}$ abundance ratios, we used the RADEX non-LTE model accounting for radiative transfer effects. This implied the use of the new collision rates from Wiesenfeld & Faure (2013). Also implementing distance values from trigonometric parallax measurements for our sources, we obtain a linear fit of $^{12}\text{C}/^{13}\text{C} = (5.08 \pm 1.10)D_{GC} + (11.86 \pm 6.60)$, with a correlation coefficient of 0.58. D_{GC} refers to Galactocentric distances. Our $^{12}\text{C}/^{13}\text{C}$ ratios agree very well with the ones deduced from CN and C^{18}O but are lower than those previously reported on the basis of H_2CO , tending to suggest that the bulk of the H_2CO in our sources was formed on dust grain mantles and not in the gas phase.

Keywords: ISM: abundances - ISM: HII regions - Galaxy: evolution

1. INTRODUCTION

Isotope abundance ratios provide a powerful tool to trace stellar nucleosynthesis, to evaluate the enrichment of the interstellar medium (ISM) by stellar ejecta and to constrain the chemical evolution of the Milky Way (Wilson & Rood 1994). In particular, the $^{12}\text{C}/^{13}\text{C}$ ratio is one of the most useful tracers of the relative degree of primary to secondary processing. ^{12}C is known to be produced primarily via Helium burning in massive stars, on rapid time scales, whereas ^{13}C is thought to be formed primarily through CNO processing of ^{12}C seeds from earlier stellar generations. This occurs on a slower timescale during the red giant phase in low and intermediate-mass stars or novae (Henkel et al. 1994, Meyer 1994; Wilson & Rood 1994). Thus the $^{12}\text{C}/^{13}\text{C}$ ratio is expected to decrease with time and a $^{12}\text{C}/^{13}\text{C}$ gradient should exist with Galactocentric distance, assuming an inside-out formation scenario of the Milky way (Pilkington et al. 2012).

Under certain conditions, isotope abundance ratios can be effectively determined from the strengths of corresponding molecular lines (e.g., H_2CO , CO and CN). Measurements of absorption lines of H_2CO and H_2^{13}CO toward strong continuum sources are believed to be one of the best ways to determine the isotope ratio between ^{12}C and ^{13}C . Previous observations support the existence of a gradient of $^{12}\text{C}/^{13}\text{C}$, i.e., the ratio increases as a function of Galactocentric distance (Wilson et al. 1976; Gardner & Whiteoak 1979; Henkel et al. 1980,1982,1983,1985). A $^{12}\text{C}/^{13}\text{C}$ ratio cannot be directly deduced from ^{12}CO (hereafter CO) and ^{13}CO , since CO (and sometimes ^{13}CO) is optically thick. Therefore, their isotopologues C^{18}O and $^{13}\text{C}^{18}\text{O}$, exhibiting optically thin lines, are sometimes used to determine $^{12}\text{C}/^{13}\text{C}$ (Langer & Penzias 1990). However, this is time-consuming, since thermally excited emission lines with low optical depths can have extremely low intensities (Wilson & Rood 1994). CN is also a tracer of the $^{12}\text{C}/^{13}\text{C}$ ratio. Although CN has a distinct hyperfine structure, which can be used to directly evaluate opacities (Savage et al. 2002; Milam et al. 2005), it is still difficult to obtain a true $^{12}\text{C}/^{13}\text{C}$ value from $^{12}\text{CN}/^{13}\text{CN}$ because of sometimes large opacities of ^{12}CN . Milam et al. (2005) proposed a gradient of $^{12}\text{C}/^{13}\text{C}$ with Galactocentric distance, from a combination of all previously published measurements of CN , C^{18}O and H_2CO . The goal of our study is to critically review their results using new distances and H_2CO collision rates as well as a larger sample of sources and to examine in how far previous results have to be modified.

Thus we have performed a more systematic study of H_2CO and H_2^{13}CO toward a big sample of Galactic molecular clouds to determine $^{12}\text{C}/^{13}\text{C}$ isotope ratios more accurately. Based on a TMRT formaldehyde survey at C-band (~ 5 GHz; Li et al. 2019, in preparation), we chose sources with strong H_2CO signals as our targets for deep integration. Some previously studied strong H_2CO sources with absolute flux densities larger than 0.5 Jy (Wilson et al. 1976; Henkel et al. 1982,1983,1985; Araya et al. 2007) are also included in our sample. H_2CO collision rates were taken from Wiesenfeld & Faure (2013) who consider H_2CO collisions with H_2 based on the high accuracy potential energy surface introduced by Troscompt et al. (2009). These rates differ significantly from the scaled rates of H_2CO in collision with He (Green et al. 1991) used in previous analyses. At the same time we also took improved distances for our sources to evaluate more accurately the previously reported gradient of the carbon isotope ratio as a function of Galactocentric distance. In Section 2, the observations of our large sample are described, encompassing Galactocentric radii from 0 to 10.5 kpc. In Section 3, we first perform the analysis of spectra and the radio continuum, followed by modelling work based on radiative transfer calculations. Section 4 provides discussions on the isotope ratio gradient, derived from our observational data alone as well as also including previously obtained data. Our main results are summarized in Section 5.

2. OBSERVATIONS

The $1_{10} - 1_{11}$ and $2_{11} - 2_{12}$ transitions were observed toward our sources in March and October 2016 as well as in May and July 2017 with the Shanghai Tianma Radio Telescope (TMRT). We used two cryogenically cooled receivers covering the frequency ranges of 4.0-8.0 GHz (C-band) and 12.0-18.2 GHz (Ku-band). The rest frequencies of the $1_{10} - 1_{11}$ transitions of H_2^{12}CO and H_2^{13}CO were set to be 4.829660 and 4.593089 GHz, respectively (Tucker et al. 1971; Wilson et al. 1976). 14.48848 GHz was adopted for the $2_{11} - 2_{12}$ transition of H_2^{12}CO . The beam sizes are ~ 4 arcmin at 5 GHz and ~ 1.3 arcmin at 14.5 GHz, respectively. A Digital Backend System (DIBAS) was used for data recording (see Li et al. 2016). The DIBAS mode 22 was adopted for our observations, with eight spectral windows, to cover the H_2^{12}CO and H_2^{13}CO lines simultaneously, each with 16384 channels and a bandwidth of 23.4 MHz, supplying channel widths of 0.09 km s^{-1} and 0.03 km s^{-1} at 5 GHz and 14.5 GHz, respectively. The system temperature was 20-30 and 30-80 K on a T_A^* scale for the $1_{10} - 1_{11}$ and $2_{11} - 2_{12}$ transition observations, respectively. The active surface system of the primary dish and a subreflector were used to improve the aperture efficiency during our Ku-band

observations. We measured an aperture efficiency of about 55 per cent (Chen et al. 2017; Dong et al. 2018a) at both the C-band and Ku-band. The spectra were obtained in a position switching mode with total on source integration times of 0.3 - 3 hours and 2 - 40 mins for the $1_{10} - 1_{11}$ and $2_{11} - 2_{12}$ transition observations, respectively. Observational parameters of our sample are listed in Appendix A.

Among our 112 targets, 84 sources were successfully detected in the $1_{10} - 1_{11}$ line of H_2CO , and 38 sources of these 84 were also successfully detected in the $1_{10} - 1_{11}$ line of H_2^{13}CO . Subsequently we observed the $2_{11} - 2_{12}$ lines of H_2CO for these 38 sources and all were detected. 5 sources are showing two velocity components. Thus, 43 radial velocity components were detected towards these 38 sources. The Signal-to-Noise (S/N) ratios of the $1_{10} - 1_{11}$ line of H_2CO are greater than 25 for these 38 sources. For the $1_{10} - 1_{11}$ line of H_2^{13}CO and the $2_{11} - 2_{12}$ line of H_2CO , the corresponding S/N ratios are greater than 5. To determine apparent optical depths, complementary observations for their continuum at both C- and Ku-bands were performed toward those 38 sources, from 2017 October 26 to November 4 and during 2018 February 4 to 8. We used the C- and Ku-band receivers, centered at 4.829660 GHz and 14.48848 GHz with 500 MHz bandwidth, respectively. A cross-scan mode was used for observations, where the antenna beam pattern was driven repeatedly in right ascension (RA) and declination (Dec) over the source position. The data were acquired with the DIBAS backend system. Before observing each target source, we chose one calibration source (e.g., 3C147, 3C295, 3C358, 3C401, 3C383 or NGC7027) near the target source to observe it for pointing correction of the telescope. We took one and two scans for calibration and target sources, respectively, with scan lengths of three minutes each. C- and Ku-band receiver features were observed with left and right circular polarization and were subsequently averaged. The continuum at both C- and Ku-bands was successfully detected toward 32 of the 38 sources. For the other 6 sources, the continuum at C-band was detected, while no Ku-band signal was obtained. 4 sources remained undetected, while 2 sources (Mol12, J205703.98) were not observed at Ku-band. Table 1 presents obtained continuum temperatures. The typical rms value of the continuum at Ku-band for the 4 undetected targets was ~ 0.1 K (~ 0.15 Jy, see below), which is also listed in Table 1. The two unobserved targets are marked by "-". Nevertheless, this does not affect our main results (see details in Sect. 3.3).

The noise diode signal inserted into the receiver system may differ slightly between the C-band frequencies of H_2CO and H_2^{13}CO . Thus we performed separate flux calibration observations at 4.829 GHz and 4.593 GHz, respectively, in January 24 to 29, 2019. Also for comparisons, we made repeated observations toward several strong sources (W3IRS5, NGC2024, SgrB2, W33) in our sample. The new results related to those strong sources are consistent with our previous ones. Based on the frequency dependencies of the spectral flux densities in Perley & Butler (2013), the radio sources 3C123, 3C147, 3C196 and 3C295 were taken as calibrators in our observations. The cross scan mode with a bandwidth of 10 MHz was used for calibrations at 4.829 GHz and 4.593 GHz and the telescope gains are 1.49 Jy K^{-1} and 1.28 Jy K^{-1} , respectively. Thus a correction factor of $(1.49/1.28)$ from the different gains at 4.829 GHz and 4.593 GHz should be applied to obtain the accurate value of the isotope abundance ratio (see details in Sect. 3.1). For C- (~ 5 GHz) and Ku-band (~ 14.5 GHz), the sensitivities are both 1.5 Jy K^{-1} . The calibrators were observed at suitable elevations of $40^\circ - 60^\circ$, while the elevation range of all the target sources is $20^\circ - 80^\circ$. Beside noise, the uncertainty of the measured flux density is mainly caused by the elevation-dependent gain curve of the TMRT (Dong et al. 2018b; see also Sect. 3.1).

3. DATA REDUCTION AND RESULTS

3.1. Optical Depth and Column Density

We used the GILDAS/CLASS package to reduce the spectral line data. A first order polynomial was subtracted from each spectrum for baseline removal. Then we obtained the line parameters via Gaussian fitting for those 38 sources, which are presented in Table 1. The spectra of the $2_{11} - 2_{12}$ lines of H_2^{12}CO , as well as the $1_{10} - 1_{11}$ lines of H_2^{12}CO and H_2^{13}CO , after subtracting baselines and applying Hanning smoothing, are shown in Figure 1. For those 46 sources with only a detection of the H_2CO $1_{10} - 1_{11}$ line, spectra and line parameters derived from Gaussian fitting are presented in Appendices B and C, respectively.

The continuum data calibration was obtained with the following procedure: First, baselines were subtracted, being defined by the lengths of the continuum scans avoiding the source itself at $\pm 1.5 \times \text{HPBW}$ (half power beam width), relative to the center of the scan. Second, Gaussian profiles were fitted to obtain the position offset between the real position of the source and the center of the cross scans. Then, the obtained amplitude was corrected for the pointing error, adopting a two-dimensional Gaussian intensity profile, using the formula:

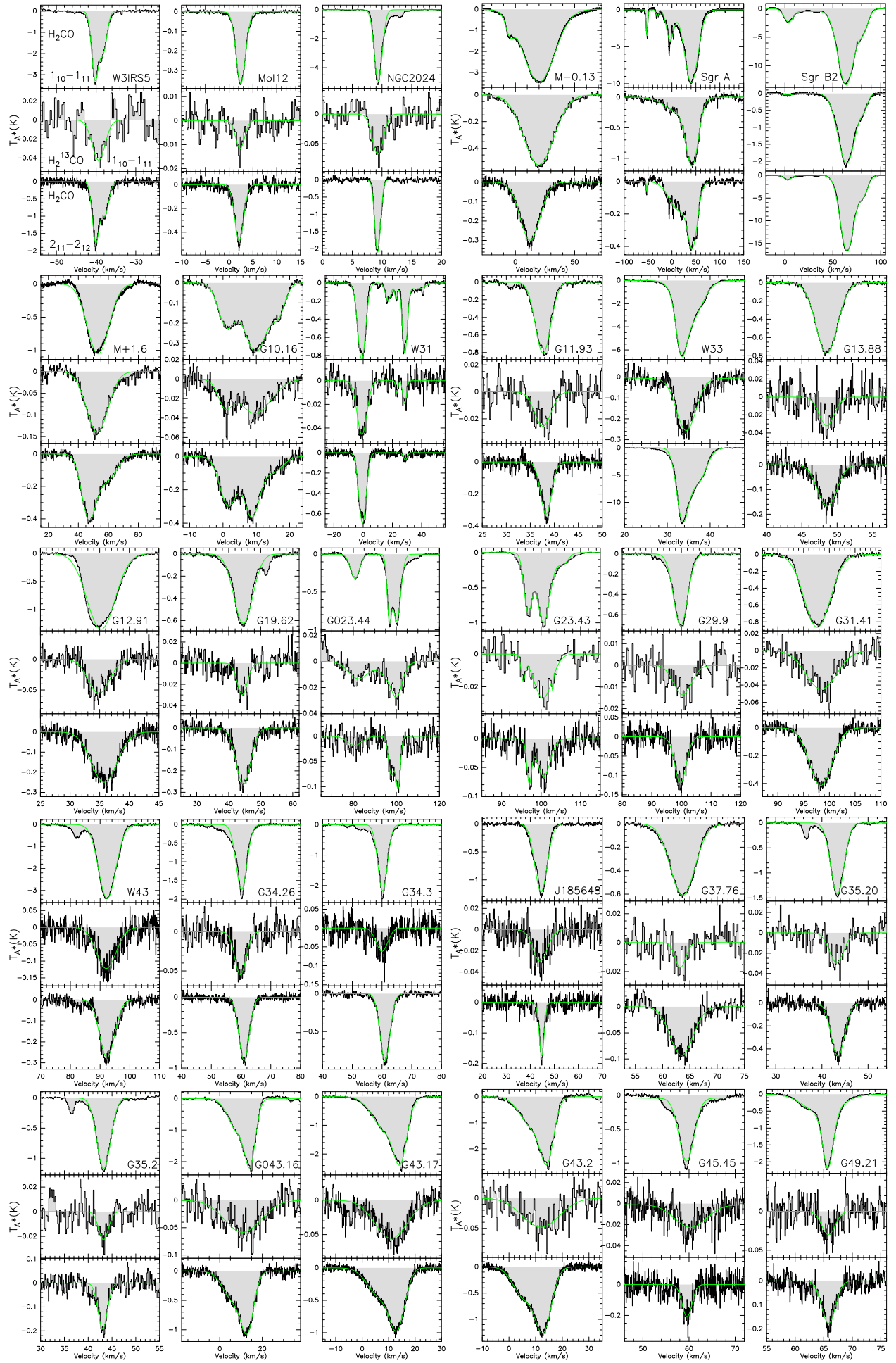
$$T_A^{*'} = T_A^* / \text{Pointing}, \quad (1)$$

Table 1. Line Parameters derived from Gaussian-fitting

Source	$1_{10} - 1_{11}$ transitions							$2_{11} - 2_{12}$ transitions		
	Continuum	H_2^{12}CO Parameters			H_2^{13}CO Parameters			H_2^{12}CO Parameters		
	antenna	Line	Full Width	V_{LSR}	Line	Full Width	V_{LSR}	Continuum	Line	Apparent
	temp.	antenna	to		antenna	to		antenna	optical	
	(K)	temp.	Half Power	(km s^{-1})	temp.	Half Power	(km s^{-1})	temperature	depth	
(1)	(2)	(3)	(4)	(5)	(6)	(7)	(8)	(9)	(10)	(11)
W3IRS5	38.8	-3 ± 0.048	3.49	-39.6	-0.035 ± 0.019	2.08	-38.6	31.5	-1.55	0.05
Mol12	0.12	-0.366 ± 0.005	2.37	2.46	-0.012 ± 0.006	2.21	2.31	-	-0.47	-
NGC2024	26.5	-4.926 ± 0.025	1.59	9.39	-0.062 ± 0.021	2.22	9.30	1.7	-2.1	1.34
M-0.13	8.79	-3.388 ± 0.041	33.55	19.19	-0.526 ± 0.032	30.16	19.75	1.3	-0.29	0.14
SgrA	79.3	-9.317 ± 0.099	38.17	39.64	-1.078 ± 0.099	37.23	40.11	4.3	-0.38	0.07
Sgr B2	20.1	-2.255 ± 0.048	14.33	4.71	-0.061 ± 0.024	8.16	2.56	54.6	-0.9	0.02
		-12.75 ± 0.048	24.79	64.91	-1.991 ± 0.024	22.96	64.93		-16.0	0.34
M+1.6	0.3	-1.054 ± 0.023	17.07	53.13	-0.140 ± 0.017	17.12	52.65	$< 0.1^*$	-0.29	> 0.11
G10.16-0.35	4.55	-0.167 ± 0.014	5.12	0.55	-0.044 ± 0.008	0.68	1.11	15.9	-0.32	0.02
		-0.325 ± 0.014	11.90	10.28	-0.021 ± 0.008	7.45	9.18		-0.24	0.01
W31	3.77	-0.842 ± 0.012	6.41	-1.02	-0.046 ± 0.010	8.09	-0.81	8.7	-0.69	0.07
		-0.748 ± 0.012	4.40	28.51	-0.020 ± 0.010	3.08	28.37		-0.07	0.007
G11.93-0.61	1.27	-0.808 ± 0.014	3.78	37.67	-0.026 ± 0.012	4.18	37.60	2.5	-0.32	0.1
W33	20.8	-6.3 ± 0.034	5.44	34.15	-0.251 ± 0.026	5.61	34.44	4.5	-12.05	-
G13.88+0.28	3.67	-0.772 ± 0.015	3.59	48.52	-0.032 ± 0.013	2.55	48.54	4.8	-0.17	0.03
G12.91-0.26	2.23	-1.354 ± 0.015	5.58	35.23	-0.056 ± 0.010	4.2	34.88	0.8	-0.25	0.16
G19.62-0.23	4.2	-0.649 ± 0.010	6.40	44.45	-0.03 ± 0.009	3.85	44.24	0.76	-0.26	0.15
G023.44-00.18	5.19	-0.324 ± 0.009	5.09	80.81	-0.016 ± 0.011	15.33	83.03	0.5	-0.02	0.01
		-0.917 ± 0.009	6.62	98.97	-0.027 ± 0.011	7.89	99.58		-0.1	0.06
G23.43-0.21	5.19	-0.88 ± 0.006	7.47	99.54	-0.026 ± 0.006	7.51	100.31	1.9	-0.05	0.02
G29.9-0.0	7.1	-0.707 ± 0.008	5.61	99.74	-0.012 ± 0.010	7.91	100.5	0.45	-0.12	0.08
G31.41+0.31	1.02	-0.864 ± 0.013	5.99	97.65	-0.045 ± 0.012	7.18	98.4	1.8	-0.42	0.19
W43	26	-3.367 ± 0.029	6.85	92.39	-0.122 ± 0.025	7.78	92.09	$< 0.1^*$	-0.27	> 0.25
G34.26+0.15	3.07	-1.738 ± 0.015	4.32	60.17	-0.055 ± 0.017	4.44	59.81	11.4	-0.89	0.08
G34.3+0.1	9.6	-2.170 ± 0.019	3.79	60.22	-0.062 ± 0.017	4.64	59.98	1.6	-0.88	0.4
J185648.26	2.44	-1.212 ± 0.016	6.14	44.47	-0.029 ± 0.013	6.90	44.08	0.3	-0.17	0.15
G37.76-0.20	3	-0.612 ± 0.010	5.33	63.68	-0.017 ± 0.011	2.31	63.25	1.79	-0.1	0.03
G35.20-1.74	13.6	-1.406 ± 0.018	3.44	43.35	-0.022 ± 0.013	4.58	43.11	16.1	-0.46	0.03
G35.2-1.8	11.2	-1.169 ± 0.328	3.44	43.26	-0.023 ± 0.011	2.41	43.22	1.8	-0.19	0.07
G043.16+00.01	34.5	-2 ± 0.045	10.26	12.46	-0.06 ± 0.020	20.43	11.06	33	-0.99	0.03
G43.17+0.00	37.5	-2.151 ± 0.016	10.64	12.49	-0.055 ± 0.017	14.2	10.93	12	-0.88	0.07
G43.2+0.0	30.4	-2.368 ± 0.061	9.81	12.67	-0.031 ± 0.019	9.1	12.84	3.58	-1.15	0.28
G45.45+0.06	7.18	-0.907 ± 0.013	4.37	59.44	-0.025 ± 0.010	4.29	60.22	2.1	-0.63	0.22
G49.21-0.35	9.7	-1.976 ± 0.014	3.31	65.69	-0.03 ± 0.015	2.78	65.84	0.87	-0.17	0.09
J192311.17	12.7	-0.548 ± 0.018	4.62	50.63	-0.025 ± 0.012	1.39	51.05	11	-0.22	0.02
		-2.924 ± 0.018	4.41	63.34	-0.039 ± 0.012	5.93	63.43		-0.27	0.022
G49.4-0.3	13.7	-2.804 ± 0.014	4.41	63.36	-0.037 ± 0.015	4.21	63.08	1.14	-0.19	0.09
G49.5-0.4	54.2	-6.212 ± 0.039	7.94	65.64	-0.144 ± 0.051	13.45	63.89	6.18	-0.79	0.11
J192345.73	35.5	-1.188 ± 0.019	8.31	57.08	-0.064 ± 0.026	12	57.16	$< 0.1^*$	-0.18	> 0.15
		-4.014 ± 0.019	6.55	66.39	-0.087 ± 0.026	6.16	66.77		-0.15	> 0.13
J203901.04	18.1	-3.84 ± 0.022	3.75	-2.608	-0.079 ± 0.033	2.06	-2.24	25.5	-1.94	0.08
DR21	15.2	-4.208 ± 0.018	3.74	-2.61	-0.0786 ± 0.019	2.06	-2.42	3.5	-2.05	0.6
J205658.56	0.13	-0.71 ± 0.015	3.29	0.84	-0.037 ± 0.013	1.81	1.13	$< 0.1^*$	-0.25	> 0.09
J205703.98	0.06	-0.804 ± 0.014	3.05	1.15	-0.041 ± 0.012	1.28	1.13	-	-0.15	-

*The typical rms values of the continuum at Ku-band for undetected sources was ~ 0.1 K.

NOTE— Column (1): source name; Column (2): continuum temperatures at 4.8 GHz; Columns (3), (4) and (5): line temperatures, FWHP line widths and $\text{H}_2\text{CO } 1_{10} - 1_{11}$ line center velocities, respectively; Columns (6), (7) and (8): $\text{H}_2^{13}\text{CO } 1_{10} - 1_{11}$ line temperatures, FWHP line widths, and line center velocities; Column (9): 14.5 GHz continuum temperatures; Column (10): $\text{H}_2^{12}\text{CO } 2_{11} - 2_{12}$ line temperatures; Column (11): apparent optical depths of the $\text{H}_2^{12}\text{CO } 2_{11} - 2_{12}$ lines.



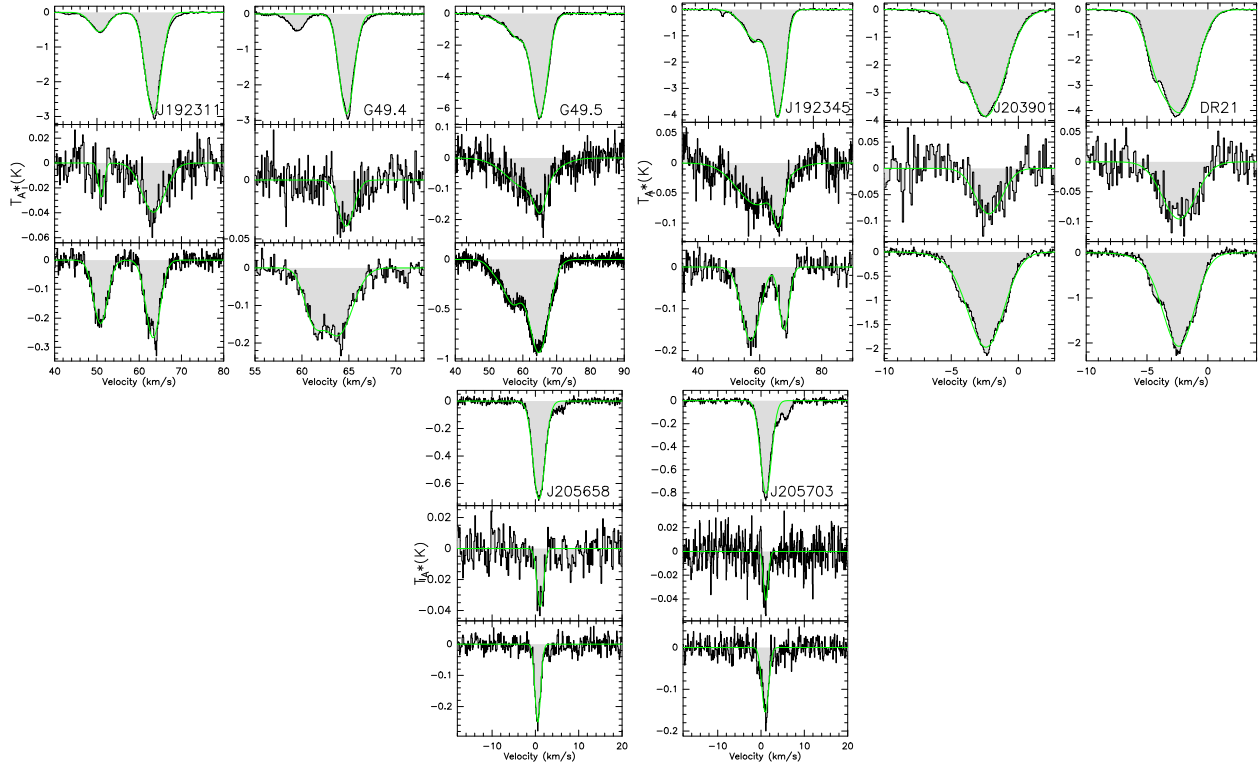


Figure 1. The $1_{10} - 1_{11}$ and $2_{11} - 2_{12}$ spectra of 38 sources, after subtracting baselines and applying Hanning smoothing. The upper profiles are the $1_{10} - 1_{11}$ transitions of H_2^{12}CO ; the middle profiles are the $1_{10} - 1_{11}$ transitions of H_2^{13}CO and the lower profiles are the $2_{11} - 2_{12}$ transitions of H_2^{12}CO . Antenna temperature scales are presented on the left hand side of the profiles.

where $Pointing = \exp(-4 \times \ln 2 \times (offset/HPBW)^2)$. Finally, the antenna temperature has been corrected for the elevation-dependent gain, defined by the parabolic equation:

$$T = T_A' / Gain, \quad (2)$$

where $Gain = A \times Elevation^2 + B \times Elevation + C$. A, B, C are the coefficients of a 2nd order polynomial fit, obtained from " $T/T_{max} - Elevation$ " plots of well-known stable calibrators (e.g. 3C286, 3C123 and 3C48). For Ku-band observations the last step of the data reduction was omitted because of an absence of a gain curve equation for this band, which provides up to 10% of uncertainty. The resulting measured amplitude of each source is an average from all its scans, in units of antenna temperature in Kelvin (K). The measurement uncertainty is formed by the statistical errors of the Gaussian fits. Figure 2 shows one example characterizing our sample of observed sources. The line parameters and continuum temperatures are listed in Table 1.

Then we used these parameters to calculate optical depths (Güsten et al. 1985)

$$\tau = -\ln(1 + T_L / (T_C + T_{BB} - T_{ex})), \quad (3)$$

where T_L is the observed line temperature, T_C is the continuum temperature, T_{BB} is the 2.7 K background radiation, and T_{ex} is the excitation temperature. We have used the RADEX non-LTE model¹ (Van der Tak et al. 2007) to provide excitation temperatures for our sources (see details in Section 3.2). The apparent maximum optical depths τ , which are the optical depths at the velocities with the most negative (absorption) line temperatures, in the $2_{11} - 2_{12}$ transition of H_2^{12}CO are listed in Table 1. In Table 2, the apparent maximum optical depths of the $1_{10} - 1_{11}$ transitions are listed. Finally, we can get with the velocity integrated optical depth the column density, following Wilson et al. (1976):

$$N_1 [cm^{-2}] = 1.26 \times 10^{13} T_{ex} \int \tau(V) dV. \quad (4)$$

¹ <http://var.sron.nl/radex/radex.php>

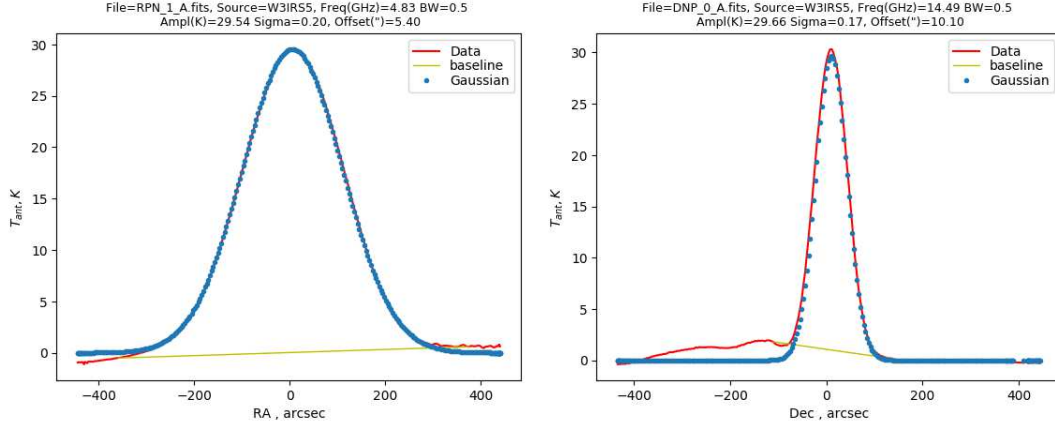


Figure 2. Continuum cross scan of W3IRS5 at 4.8 GHz(left) and 14.5 GHz (right). Red: observed cross scans. Blue: Gaussian fits. Yellowish: First order baseline fits to the measured data.

The radial velocity V is in km s^{-1} and the excitation temperature T_{ex} in K. The numerical coefficient is valid for H_2^{12}CO ; the coefficient for H_2^{13}CO is 1.32×10^{13} . The column densities in the 1_{11} level divided by the a priori unknown quantity T_{ex} for our sources are listed in Columns 6 and 7 of Table 2. Used velocity ranges are given in Columns 4 and 5.

We derived the $\text{H}_2^{12}\text{CO}/\text{H}_2^{13}\text{CO}$ isotope ratios in two different ways: (1) from Gaussian least square fits and (2) using planimetry to derive the ratio of their column densities (Col.(8) of Table 2; see details in Wilson et al. 1976). Since the ratios obtained by these two methods differ by only 10% within the permissible margin of error, we average these two ratios to get the final $\text{H}_2^{12}\text{CO}/\text{H}_2^{13}\text{CO}$ ratios. The average ratios corrected for telescope gain (see details in Section 2) for our sample are listed in Col.(4) of Table 3.

3.2. Beam Size Effect

The beam sizes are ~ 4 arcmin at C-band and ~ 1.3 arcmin at Ku-band, respectively. The temperature difference between the microwave background (2.73 K) and the excitation temperature of the collisionally cooled (Evans et al. 1975) H_2CO lines is about 1.5 K, as derived from our non-LTE calculations. For a cloud fully filling the beam, and being optically moderately thin, e.g. $\tau = 0.3$, this would result in about 0.5 K across that part of the beam not covered by a background HII region. Assuming that the HII region has a diameter of 6 arcsec (e.g., Zapata et al. 2009) and a radiation temperature of 6000 K (e.g., Reifenstein et al. 1970), we obtain for $T_{\text{non-HII-region}}(\text{H}_2\text{CO})/T_{\text{HII-region}}(\text{H}_2\text{CO})$ values of about 0.01 and 0.1 for a 1.3 arcmin beam and 4 arcmin beam, respectively. The result indicates that in this case the tiny spot in front of the HII region dominates the H_2CO absorption budget and the difference in beam sizes can be neglected. If the respective clouds are not filling the entire 4 arcmin beam, the comparatively small area covered by the continuum emission becomes even more dominant and the difference in beam size can also be neglected.

3.3. Photon Trapping Corrections

Photon trapping in the millimeter H_2CO rotation lines, connecting the $J = 1$ and 2 K-doublets (i.e. the $2_{11} - 1_{10}$ and $2_{12} - 1_{11}$ transitions), has also to be considered. In case the two millimeter lines ($2_{11} - 1_{10}$ and $2_{12} - 1_{11}$) are not entirely optically thin, their excitation temperature values rise and are higher than in the optically thin case, represented by H_2^{13}CO . Thus, more population ends up in the H_2CO $J = 2$ doublet than in the entirely optically thin case represented by H_2^{13}CO . The $J = 1$ H_2CO doublet then gets a little depopulated and thus the C-band $\text{H}_2\text{CO}/\text{H}_2^{13}\text{CO}$ line intensity ratio becomes smaller than if both H_2CO and H_2^{13}CO lines were all optically thin. Here, the RADEX non-LTE model¹ was used to correct the ratios for photon trapping. As already mentioned in Sect. 1, the collision rates of H_2CO are taken from Wiesenfeld & Faure (2013), which are calculated for H_2CO in collision with H_2 and the high accuracy potential energy surface of Troscompt et al. (2009). These are significantly different from the scaled rates of H_2CO in collision with He (Green et al. 1991; see below). Correction factors $f_{12/13}$ calculated by the new collision rates tend to be larger than those derived by the old collision rates, especially for larger optical depths at 4.8 GHz, as shown in Figure 3. The correction factor $f_{12/13}$ is defined as in Henkel et al. (1980):

$$f_{12/13} = 50\tau_{4.8}^0/\tau_{4.8}^*, \quad (5)$$

Table 2. $\text{H}_2^{12}\text{CO}/\text{H}_2^{13}\text{CO}$ isotope ratios obtained with the planimetry method

Source	Apparent maximum optical depth		Velocity range used for integrated optical depth		$\int_{V_1}^{V_2} \frac{N_1 dV}{T_{ex}}$	$R = \frac{col.(6)}{col.(7)}$	Distance of cloud from Galactic center	
	H ₂ ¹² CO	H ₂ ¹³ CO	V ₁	V ₂	H ₂ ¹² CO	H ₂ ¹³ CO		
				(km s ⁻¹)	(10 ¹³ cm ⁻² K ⁻¹)	(10 ¹¹ cm ⁻² K ⁻¹)	(kpc)	
(1)	(2)	(3)	(4)	(5)	(6)	(7)	(8)	(9)
W3IRS5	0.088	0.0018	-44	-34	0.353 ± 0.002	0.464 ± 0.082	76 ± 14	10.3
Mol12	0.464	0.0221	-1	8	1.401 ± 0.008	4.698 ± 0.839	30 ± 5	9.71 ^a
NGC2024	0.205	0.0024	7	15	0.465 ± 0.001	0.778 ± 0.100	60 ± 7.9	7.22
M-0.13	0.431	0.0615	-25	71	17.47 ± 0.021	229.8 ± 1.521	7.6 ± 0.06	0.06
SgrA	0.132	0.0166	4	91	5.01 ± 0.004	6.964 ± 0.401	9.1 ± 0.05	0.17
Sgr B2	0.116	0.0043	-13	23	1.83 ± 0.025	1.829 ± 0.427	100 ± 25	7.81
	0.933	0.108	37	103	25.48 ± 0.002	311.97 ± 0.469	8.2 ± 0.01	0.38 ^a
M+1.6	0.943	0.106	30	85	17.8 ± 0.296	204.3 ± 22.71	8.7 ± 0.97	0.77
G10.16-0.35	0.063	0.0105	-8	4	1.32 ± 0.005	5.54 ± 0.646	24 ± 3	7.44
	0.281	0.0135	4	23	3.48 ± 0.006	10.56 ± 0.693	33 ± 2	6.24
W31	0.164	0.0111	-13	7	1.42 ± 0.001	10.35 ± 0.058	14 ± 0.1	3.38 ^a
	0.160	0.006	24	36	0.902 ± 0.001	1.568 ± 0.058	58 ± 2	5.0
G11.93-0.61	0.45	0.022	32	43	2.08 ± 0.021	6.144 ± 1.282	34± 7	4.88 ^a
W33	0.344	0.0135	25	43	2.26 ± 0.002	9.94 ± 0.140	23 ± 1	5.32 ^a
G13.88+0.28	0.17	0.0094	43	54	0.77 ± 0.004	1.87 ± 0.353	41 ± 8	4.41 ^a
G12.91-0.26	0.506	0.0253	28	43	3.61 ± 0.015	9.49 ± 0.748	38 ± 3	5.69 ^a
G19.62-0.23	0.124	0.008	32	50	1.17 ± 0.007	5.3 ± 0.779	22 ± 3	5.23
G023.44-00.18	0.05	0.0049	70	87	0.32 ± 0.004	5.1 ± 0.623	6 ± 1	2.48
	0.155	0.0065	90	115	1.31 ± 0.005	4.35 ± 0.473	30 ± 3	3.59 ^a
G23.43-0.21	0.174	0.005	90	113	1.4 ± 0.005	3.83 ± 0.445	37 ± 4	3.9
G29.9-0.0	0.088	0.0042	86	108	0.666 ± 0.003	1.3 ± 0.257	51 ± 10	4.38
G31.41+0.31	0.654	0.0478	88	107	4.71 ± 0.050	24.3 ± 1.934	19 ± 2	4.51
W43	0.131	0.0059	84	103	1.16 ± 0.002	4.12 ± 0.167	28 ± 1	4.58
G34.26+0.15	0.655	0.018	47	68	3.24 ± 0.011	9.27 ± 0.958	35 ± 4	5.58
G34.3+0.1	0.251	0.0087	53	68	1.22 ± 0.005	3.93 ± 0.497	31 ± 4	5.58
J185648.26	0.45	0.0153	35	54	3.18 ± 0.015	8.55 ± 1.010	37 ± 5	4.8
G37.76-0.20	0.153	0.0076	55	71	1.05 ± 0.004	0.89 ± 0.415	118 ± 55	5.62
G35.20-1.74	0.104	0.0034	38	49	0.46 ± 0.002	1.07 ± 0.145	43 ± 6	5.77 ^a
G35.2-1.8	0.1	0.0029	38	48	0.45 ± 0.046	0.92 ± 0.159	49 ± 14	6.16
G043.16+00.01	0.066	0.0028	-8	23	0.78 ± 0.006	4.56 ± 0.293	17 ± 1	7.6 ^a
G43.17+0.00	0.069	0.0026	-8	24	0.83 ± 0.001	3.15 ± 0.107	26 ± 1	7.56
G43.2+0.0	0.09	0.0216	-8	24	1.04 ± 0.009	6.04 ± 0.299	17 ± 1	7.55
G45.45+0.06	0.128	0.0065	52	70	0.75 ± 0.003	3.02 ± 0.318	25 ± 3	6.39 ^a
G49.21-0.35	0.224	0.0049	58	72	0.98 ± 0.002	0.78 ± 0.240	126 ± 39	6.15
J192311.17	0.042	0.0033	44	56	0.25 ± 0.002	0.31 ± 0.155	81 ± 41	6.31
	0.246	0.0056	57	73	1.35 ± 0.002	2.19 ± 0.155	62 ± 4	6.17
G49.4-0.3	0.218	0.0037	56	73	1.49 ± 0.003	1.58 ± 0.121	94 ± 7	6.17
G49.5-0.4	0.128	0.0054	47	76	1.4 ± 0.002	5.09 ± 0.235	28 ± 1	6.18
J192345.73	0.117	0.0032	47	76	1.36 ± 0.002	4.84 ± 0.266	28 ± 2	6.18
J203901.04	0.221	0.0066	-8	2	1.05 ± 0.002	1.44 ± 0.165	73 ± 8	8.14
DR21	0.297	0.0077	-8	2	1.38 ± 0.002	2.92 ± 0.167	47 ± 3	8.05 ^a
J205658.56	0.935	0.051	-5	9	3.67 ± 0.025	12.0 ± 1.729	31 ± 5	7.38
J205703.98	1.604	0.051	-4	5	5.10 ± 0.033	11.7 ± 1.915	44 ± 7	7.37

^a From Reid et al. (2014).

NOTE—Column (1): source name; Columns (2) and (3): the apparent optical depths of H_2^{12}CO and H_2^{13}CO $1_{10} - 1_{11}$ respectively; Columns (4) and (5): the velocity range used for integrated optical depth; Columns (6) and (7): the values of the column densities in the 1_{11} level divided by T_{ex} for H_2^{12}CO and H_2^{13}CO respectively; Column (8): the $\text{H}_2^{12}\text{CO}/\text{H}_2^{13}\text{CO}$ isotope ratios obtained with the planimetry method; Column (9): the distance from the Galactic center.

where the star indicates the RADEX model and the superscript zero refers to the model with the same H_2 density and temperature but with a formaldehyde column density which is a factor 50 times lower. The results are listed in Table 3. We ran the RADEX offline code to independently estimate the H_2 density for our sources, and find in good agreement that it ranges from $10^{4.7} \text{ cm}^{-3}$ to $10^{5.3} \text{ cm}^{-3}$. An example of this fitting process (see details in Ginsburg et al. 2011) is shown in Figure 4. The H_2 density of the HII regions is $\sim 10^5 \text{ cm}^{-3}$ (Henkel et al. 1980; Ginsburg et al. 2011; Tang et al. 2017). For the 6 sources for which we only derived the upper limit of the 2_{11} - 2_{12} optical depths due to the non-detection of continuum at Ku-band, we assume that the H_2 density in these 6 sources is also $\sim 10^5 \text{ cm}^{-3}$. Thus we adopt $n(\text{H}_2) = 10^5 \text{ cm}^{-3}$ for all of our sources. In Figure 5, we show the dependence of $f_{12/13}$ on $\tau_{4.8}$ for various molecular hydrogen densities and temperatures. As expected, the corrections to the measured isotope ratios become more important with larger optical depth. As for the kinetic temperatures, molecular clouds near ultracompact HII (UCHII) regions have a temperature of around 40 K, which is warmer than the molecular environment of more evolved HII regions (Rivera-Ingraham et al. 2010; Ginsburg et al. 2011). Therefore, we chose the kinetic temperature range of 20K-40K to analyze the effect of temperature on $f_{12/13}$. The results show that there is little difference for $f_{12/13}$ in the kinetic temperature range of 20K-40K, as can be seen in Figure 5. Thus we adopt 30 K as the kinetic temperature for our sources.

3.4. Hyperfine Structure

Both the $1_{10} - 1_{11}$ H_2^{12}CO and H_2^{13}CO lines are split by hyperfine interactions (Tucker et al. 1971). The H_2^{12}CO line consists of six hyperfine components extended over 30 kHz (Kukolich & Rubin 1971; Johnson et al. 1972; Gardner & Whiteoak 1979), corresponding to a velocity range between -1.13 km s^{-1} and $+0.71 \text{ km s}^{-1}$ relative to the line center (4829.66 MHz). For line widths of order 1 km s^{-1} , the line profile can be characterized by two components. 89% of the intensity go into features between -0.07 km s^{-1} and $+0.71 \text{ km s}^{-1}$, 11% into the feature at -1.13 km s^{-1} . This implies that for wider lines, 100% of the intensity can be observed. While for very narrow lines from dark clouds, the -1.13 km s^{-1} feature may be seen separately (e.g., Henkel et al. 1981). However, this did not occur in our sources. The hfs slightly broadens the H_2^{13}CO lines with respect to the H_2^{12}CO lines (Zuckerman et al. 1974). This should be taken into account. For 21 hyperfine components in the H_2^{13}CO $1_{10} - 1_{11}$ transition, 77% go into components between -1.15 km s^{-1} and $+1.15 \text{ km s}^{-1}$ relative to the line center (4593.089 MHz), while 11.5% go into -8.5 and -6.0 km s^{-1} and another 11.5% into $+5.7$ to $+8.1 \text{ km s}^{-1}$ features. Thus, in case of weakly detected H_2^{13}CO lines, we obtain only 77% of the total intensity for most of our sources. However, in case of really strong H_2^{13}CO lines, we can also see the outer features near -7 and $+7 \text{ km s}^{-1}$. Based on the different S/N ratio of each source, we derived the factors of hyperfine splitting (f_{hfs}) individually for each source. The corrections for hyperfine splitting, also accounting for the fact that H_2CO and H_2^{13}CO are measured at slightly different frequencies ($(\nu_{13}/\nu_{12}) \cdot f_{hfs}$), are listed in Column 5 of Table 3.

With corrections due to photon trapping ($f_{12/13}$), hyperfine splitting (f_{hfs}) and line frequencies, the corrected isotope ratios are derived from the measured isotope ratio R for our 38 sources (Güsten et al. 1985; Henkel et al. 1985):

$$[H_2^{12}\text{CO}]/[H_2^{13}\text{CO}] = (\nu_{13}/\nu_{12}) \cdot f_{hfs} \cdot f_{12/13} \cdot R. \quad (6)$$

For comparison, previously published ratios are also collected and are included in Table 4. There are 15 sources from $\text{H}_2\text{CO}/\text{H}_2^{13}\text{CO}$ measurements (Henkel et al. 1980,1982,1983,1985), 18 from $\text{CN}/^{13}\text{CN}$ measurements (Savage et al. 2002; Milam et al. 2005) and 9 from $\text{C}^{18}\text{O}/^{13}\text{C}^{18}\text{O}$ measurements (e.g., Langer & Penzias 1990; Wouterloot et al. 1996; Keene et al. 1998). With respect to these previous measurements, our sample of 38 sources and 43 velocity components covering a wide range of Galactocentric distances provides a significant sample for studying the radial gradient of the isotope ratio $^{12}\text{C}/^{13}\text{C}$.

3.5. Distances

Therefore, we also need Galactocentric distances for our sources that are more accurate than those used in previous less extended surveys. The trigonometric parallax is a very accurate method to measure the distance of sources, which can directly and geometrically determine source distances from the Sun (Reid et al. 2009; 2014). Based on trigonometric parallax data, Reid et al. (2014) provide an accurate method (see details in Reid et al. 2009) for estimating revised kinematic distances with improved Galactic constants and rotation curve. Thus we derived the heliocentric distance for 12 of our sources (marked in Table 2) from their trigonometric parallax data (Reid et al. 2014). For the other 26 sources without trigonometric parallax data, we estimated their heliocentric distance using the Revised Kinematic

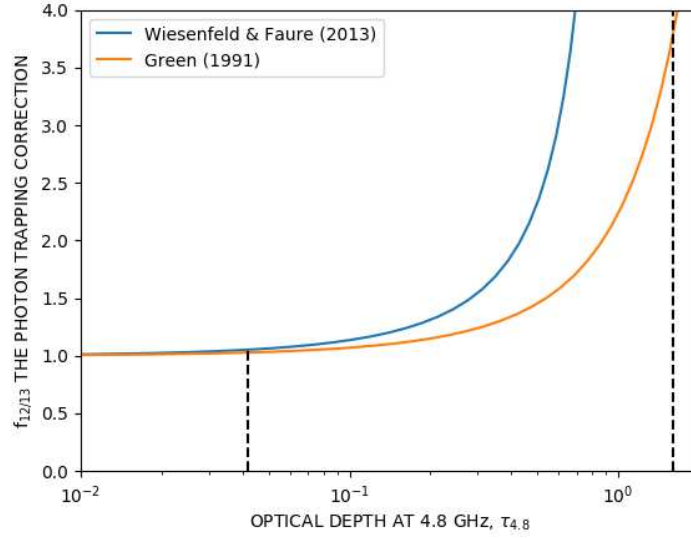


Figure 3. The comparison of $f_{12/13}$ calculated with the new collision rates (blue line; Wiesenfeld & Faure 2013) and the collision rates of Green (1991; orange line) for a kinetic temperature of 30 K and a molecular hydrogen density of 10^5 cm^{-3} . The black dotted lines indicate the range of optical depth of our sources at 4.8 GHz.

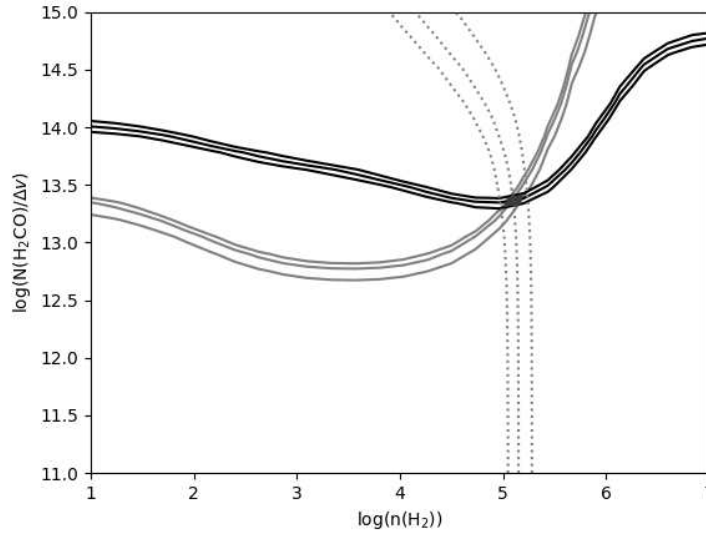


Figure 4. Determination of the H_2 density for one of our sample sources, W3-IRS5. The black and gray solid curves reproduce the $1_{10}-1_{11}$ and $2_{11}-2_{12}$ optical depths, respectively. The almost vertical gray dotted curves delineate the ratio of these two optical depths. For each of these parameters, the central line refers to the measured value, while the pair of curves around it shows the standard deviations (rms), which were calculated with the rms noise obtained from Gaussian-fitting of the $1_{10}-1_{11}$ and $2_{11}-2_{12}$ transitions. The small shaded region where the curves overlap shows the allowed parameter space for which the physical parameters are derived.

Distance Calculator², also based on the results of the parallax measurements. This also includes 7 sources, which are not part of our sample but which were included in previous measurements. A more accurate distance was adopted

² http://bessel.vlbi-astrometry.org/revised_kd_2014

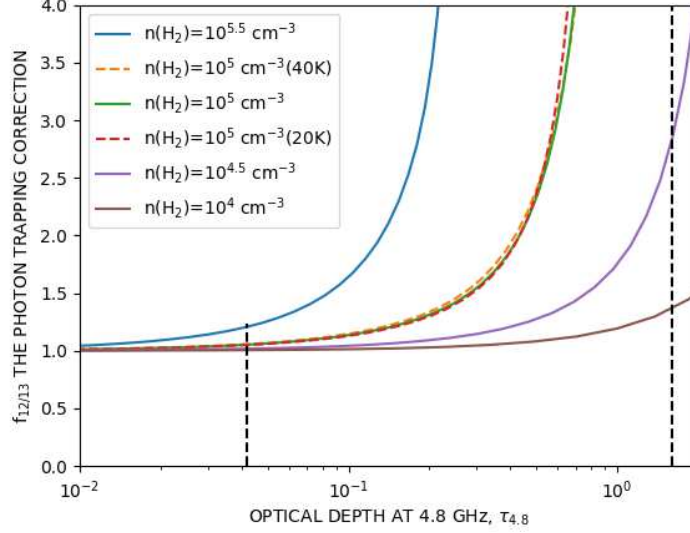


Figure 5. The full lines are curves showing the theoretical dependence of the correction factor for photon trapping $f_{12/13}$ on the 4.8 GHz optical depth of H_2^{12}CO for a kinetic temperature of 30 K, and for molecular hydrogen densities varying between 10^4 cm^{-3} and $10^{5.5} \text{ cm}^{-3}$. The dashed lines show the correction factor of two temperatures (20K, 40K) for $n(\text{H}_2) = 10^5 \text{ cm}^{-3}$. The black dotted lines indicate the range of optical depth of our sources at 4.8 GHz.

here (listed in Table 4), including 5 sources (W3-OH, W51M, Orion A, Orion Bar and NGC7538) with trigonometric parallax distances (Menten et al. 2007; Reid et al. 2014) and 2 sources (S156, WB 391) with new heliocentric distances from the Revised Kinematic Distance calculator. The latter were obtained with a solar rotational velocity of $V_0 = 240 \text{ km s}^{-1}$, assuming the derivative of the rotation curve beyond $R = R_0$ (for the solar galactocentric value, we adopted 8.125 kpc, Gravity Collaboration et al. 2018) to be $dV/dR = 0.2 \text{ km s}^{-1} \text{ kpc}^{-1}$ and the solar motion with respect to the LSR to be $(U_\odot, V_\odot, W_\odot) = (10.7, 15.6, 8.9) \text{ km s}^{-1}$ (Reid et al. 2014). Then, we can determine the Galactocentric distance from the heliocentric distance (Roman-Duval et al. 2009):

$$r = \sqrt{(R_0 \cos(l) - d)^2 + R_0^2 \sin^2(l)}, \quad (7)$$

where l is the Galactic longitude of the source and d is the kinematic distance.

The new Galactocentric distances for our 38 detected sources and 7 sources not in our sample are listed in Table 2 and Table 4, respectively.

4. DISCUSSION

With the accurate Galactocentric distance and the corrected $\text{H}_2^{12}\text{CO}/\text{H}_2^{13}\text{CO}$ ratios, we can study the variation of the $^{12}\text{C}/^{13}\text{C}$ isotope ratios as a function of Galactocentric distance. We show our results as filled black squares in Figure 6. Previous results of the ratio are also plotted, but against the new distance values (see details in Sect. 3.5), and new linear fitting lines are also presented in Figure 6. A comparison shows that using the new distances really affects the fitting results (see details in Table 5). E.g., for the gradient results from $\text{H}_2^{12}\text{CO}/\text{H}_2^{13}\text{CO}$ in Henkel et al. (1980,1982,1983,1985), the slope/intercept becomes $(8.66 \pm 1.64)/(9.30 \pm 10.37)$ from $(7.60 \pm 1.79)/(18.05 \pm 10.88)$. The fitting for $\text{CN}/^{13}\text{CN}$ in Milam et al. (2005) becomes $(6.87 \pm 1.46)/(5.06 \pm 11.07)$ from $(6.01 \pm 1.19)/(12.28 \pm 9.33)$. In addition we give in Table 5 the ratios that would be derived using the old distances and the collision rates of Green et al. (1991). It is clear that the $^{12}\text{C}/^{13}\text{C}$ gradient in the case of the collision rates taken from Wiesenfeld & Faure (2013) and new distances are closer to the gradient derived from CN and C^{18}O . In order not to bias our results towards low values with small error bars, the gradient was calculated from an unweighted least-squares fit of our corrected $\text{H}_2^{12}\text{CO}/\text{H}_2^{13}\text{CO}$ ratios with the collision rates taken from Wiesenfeld & Faure (2013) and the new, more reliable distances:

$$^{12}\text{C}/^{13}\text{C} = (5.08 \pm 1.10)D_{GC} + (11.86 \pm 6.60). \quad (8)$$

Table 3. The $^{12}\text{C}/^{13}\text{C}$ isotope ratios from corrected $\text{H}_2^{12}\text{CO}/\text{H}_2^{13}\text{CO}$ ratios

Source	Excitation temperature		Average ratios	Corrections	Corrections	Corrected Ratios
	4.8 GHz	14.5 GHz	with corrections due	for Line Frequencies	for Photon	
			to telescope gain	and Hyperfine Effects	Trapping	
	(K)	(K)		$(\nu_{13}/\nu_{12}) \cdot f_{hfs}$	$f_{12/13}$	
(1)	(2)	(3)	(4)	(5)	(6)	(7)
W3IRS5	1.21	1.56	84 ± 15	0.67	1.06	60 ± 11
Mol12	1.85	2.03	37 ± 6	0.68	1.89	47 ± 8
NGC2024	1.31	1.62	65 ± 8	0.68	1.18	52 ± 6
M-0.13	1.45	1.71	8.59 ± 0.06	0.95	1.36	11.10 ± 0.08
SgrA	1.22	1.57	10.45 ± 0.11	0.95	1.08	10.71 ± 0.11
Sgr B2	1.20	1.56	96 ± 18	0.76	1.05	77 ± 15
	1.46	1.72	8.78 ± 0.02	0.95	1.38	11.48 ± 0.03
M+1.6	1.26	1.59	9.45 ± 0.63	0.95	1.13	10.15 ± 0.68
G10.16-0.35	1.33	1.63	30 ± 5	0.66	1.21	24 ± 4
	1.35	1.64	45 ± 3	0.75	1.23	42 ± 3
W31	1.17	1.55	$21 \pm 5^*$	0.76	1.02	16 ± 4
	1.17	1.55	64 ± 7	0.71	1.02	47 ± 5
G11.93-0.61	1.69	1.90	36 ± 6	0.74	1.68	45 ± 7
W33	1.28	1.60	27 ± 1	0.74	1.15	23 ± 1
G13.88+0.28	1.31	1.62	43 ± 7	0.68	1.18	35 ± 6
G12.91-0.26	1.65	1.87	41 ± 3	0.74	1.63	49 ± 3
G19.62-0.23	1.28	1.60	34 ± 4	0.73	1.15	28 ± 3
G023.44-00.18	1.20	1.56	$23 \pm 17^*$	0.74	1.05	18 ± 13
	1.28	1.60	34 ± 3	0.76	1.15	30 ± 3
G23.43-0.21	1.28	1.60	44 ± 5	0.76	1.15	39 ± 4
G29.9-0.0	1.23	1.57	54 ± 11	0.76	1.09	44 ± 9
G31.41+0.31	1.95	2.13	21 ± 2	0.76	2.04	32 ± 2
W43	1.25	1.58	31 ± 1	0.77	1.11	26 ± 1
G34.26+0.15	1.66	1.87	38 ± 3	0.73	1.64	46 ± 4
G34.3+0.1	1.34	1.64	35 ± 4	0.74	1.22	31 ± 4
J185648.26	1.55	1.79	43 ± 4	0.75	1.49	48 ± 5
G37.76-0.20	1.30	1.62	$42 \pm 28^*$	0.69	1.18	34 ± 23
G35.20-1.74	1.23	1.58	53 ± 8	0.74	1.09	43 ± 6
G35.2-1.8	1.23	1.58	72 ± 15	0.68	1.09	53 ± 11
G043.16+00.01	1.20	1.56	$39 \pm 14^*$	0.95	1.05	39 ± 14
G43.17+0.00	1.20	1.56	$45 \pm 14^*$	0.84	1.05	40 ± 13
G43.2+0.0	1.21	1.57	$89 \pm 57^*$	0.77	1.07	72 ± 46
G45.45+0.06	1.26	1.59	36 ± 5	0.74	1.12	30 ± 4
G49.21-0.35	1.32	1.63	119 ± 29	0.69	1.20	99 ± 24
J192311.17	1.19	1.55	$26 \pm 13^*$	0.67	1.04	18 ± 9
	1.33	1.63	66 ± 5	0.75	1.20	59 ± 4
G49.4-0.3	1.34	1.64	95 ± 8	0.74	1.22	86 ± 7
G49.5-0.4	1.25	1.58	$50 \pm 18^*$	0.81	1.11	45 ± 16
J192345.73	1.24	1.58	$22 \pm 9^*$	0.81	1.10	19 ± 8
J203901.04	1.31	1.62	76 ± 8	0.71	1.18	64 ± 7
DR21	1.36	1.65	55 ± 3	0.71	1.24	48 ± 3
J205658.56	1.67	1.88	38 ± 5	0.67	1.65	42 ± 5
J205703.98	1.71	1.91	$23 \pm 7^*$	0.66	1.70	26 ± 8

* For those sources with poor H_2^{13}CO Signal-to-Noise ratios, the abundance ratios are derived from the peak value, instead of the integrated intensity.

NOTE—Column (1): source name; Columns (2) and (3): the excitation temperatures of $\text{H}_2^{12}\text{CO } 1_{10} - 1_{11}$ and $2_{11}-2_{12}$ lines derived from the RADEX model, respectively; Column (4): $\text{H}_2\text{CO}/\text{H}_2^{13}\text{CO}$ line intensity ratios (averages from values obtained by Gaussian fits and the planimetry method) corrected for differences in telescope gain; Column (5): the corrections for line frequencies and hyperfine effects; Column (6): the correction factor $f_{12/13}$ obtained from RADEX; Column (7): the corrected $\text{H}_2^{12}\text{CO}/\text{H}_2^{13}\text{CO}$ isotope ratios.

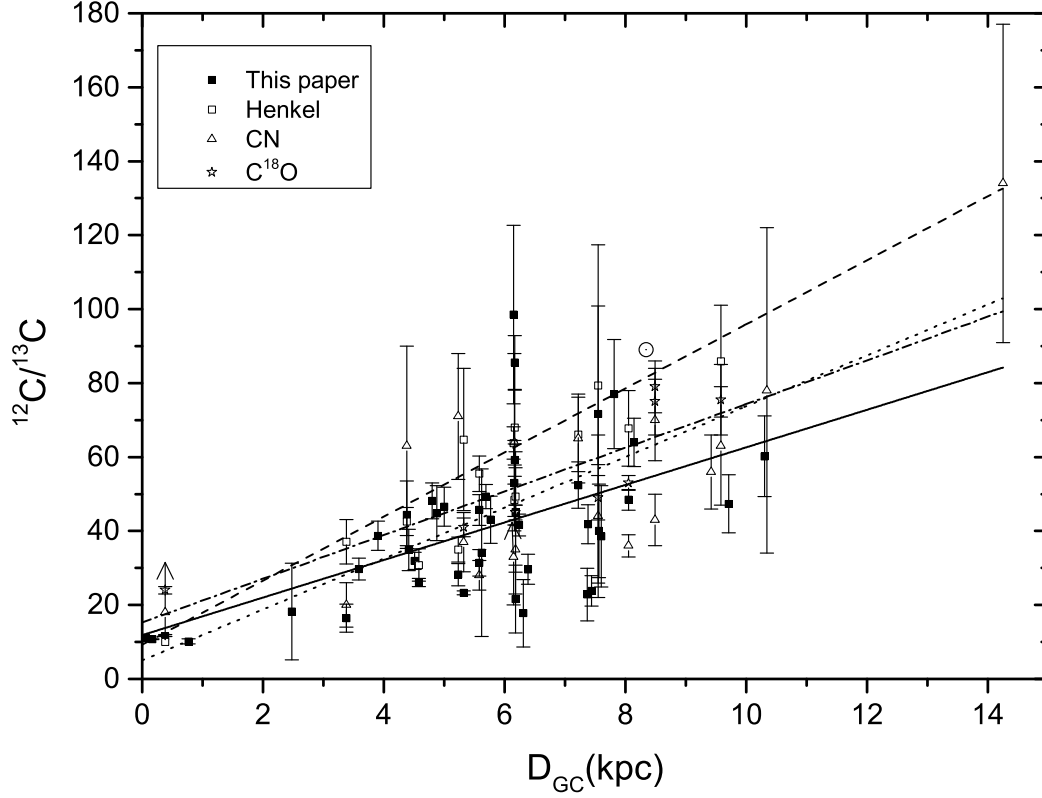


Figure 6. The $^{12}\text{C}/^{13}\text{C}$ isotope ratios from $\text{H}_2\text{CO}/\text{H}_2^{13}\text{CO}$, $\text{CN}/^{13}\text{CN}$, and $\text{C}^{18}\text{O}/^{13}\text{C}^{18}\text{O}$ plotted as functions of the distance from the Galactic center. The filled black squares are the results derived in the current work from H_2CO and the result of a first order polynomial fit is plotted as a solid line. The open squares are values derived with H_2CO from Henkel et al. (1980, 1982, 1983, 1985), using state of the art distances, and are fitted by a dashed line. The empty triangles and stars are values from CN (Savage et al. 2002, Milam et al. 2005) and C^{18}O (Langer & Penzias 1990, Wouterloot & Brand 1996, Keene et al. 1998), respectively, also using modified distances. The dotted line presents the linear fit from CN, and the dash-dotted line is the fit from C^{18}O . The symbol \odot indicates the $^{12}\text{C}/^{13}\text{C}$ isotope ratio of the Sun. All of the values are also presented in Table 4.

This gradient is flatter than the gradient derived from previous H_2CO measurements (Henkel et al. 1980, 1982) but agrees very well with those from CN and C^{18}O measurements (Milam et al. 2005).

Although our results are more reliable (due to our bigger sample, the new collision rates, more accurate distances and presumably a more realistic determination of the photon trapping effect), some other uncertainties (observational bias due to different distances, beam sizes, excitation temperatures, isotope selective photodissociation and chemical fractionation) should be mentioned.

1. Observational bias due to distance effects

The $^{12}\text{C}/^{13}\text{C}$ isotope ratios from our $\text{H}_2\text{CO}/\text{H}_2^{13}\text{CO}$ measurements plotted as functions of the distance from the Sun are shown in Figure 7. No apparent gradient can be found, which suggests that any observational bias due to distance related effects is not significant for the $^{12}\text{C}/^{13}\text{C}$ gradient as a function of Galactocentric distance.

2. Excitation temperature

We assumed that the excitation temperature of the $1_{10} - 1_{11}$ transition for H_2CO equals that for H_2^{13}CO . It is generally accepted that these lines are affected by a collisional pumping mechanism (Evans et al. 1975; Wilson et al. 1976), which should produce nearly the same excitation temperature for the two species. Hence any differences in the excitation between the two species should be negligible.

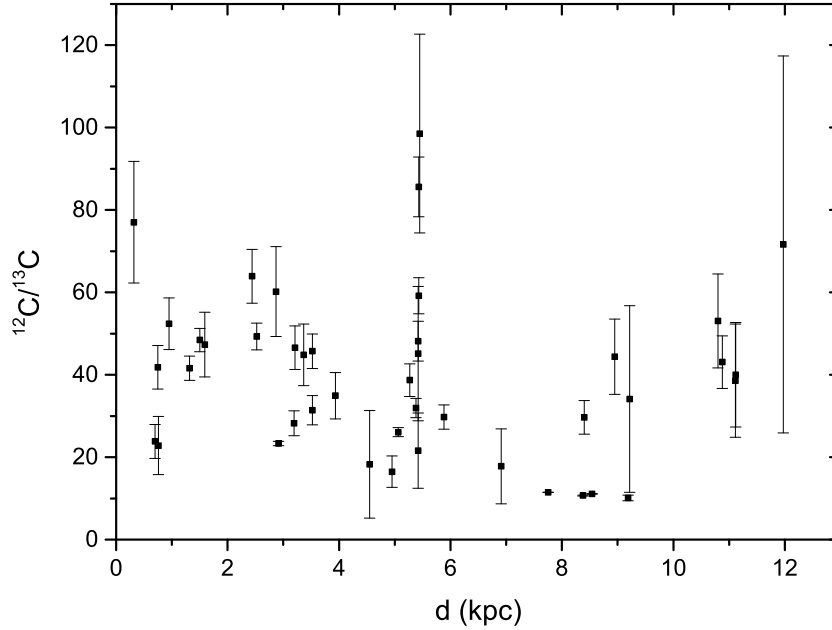


Figure 7. The $^{12}\text{C}/^{13}\text{C}$ isotope ratios from our $\text{H}_2\text{CO}/\text{H}_2^{13}\text{CO}$ measurements plotted as functions of the distance from the Sun.

3. Isotope selective photodissociation

Isotope selective photodissociation can occur in a molecular cloud affected by high UV radiation, which increases the $^{12}\text{C}/^{13}\text{C}$ isotope ratio (Riquelme et al. 2010). This effect is particularly pronounced in photon-dominated regions (PDRs). The UV photons can photodissociate the rarer isotopologues and affect less the main isotopologues (the more abundant molecules) due to their more efficient self-shielding, which would lead to higher $^{12}\text{C}/^{13}\text{C}$ isotope ratios. However, isotope selective photodissociation hardly affects the $^{12}\text{C}/^{13}\text{C}$ ratio from high density tracers like CN (Milam et al. 2005). And since the $^{12}\text{C}/^{13}\text{C}$ ratios derived from H_2CO , C^{18}O and CN are quite similar in the average (Fig. 6), isotope selective photodissociation should not be a dominant effect.

4. Chemical fractionation

In order to investigate the effects of chemical fractionation, we must understand the formation of formaldehyde (H_2CO). In classic gas-phase reaction networks, H_2CO is formed from neutral-neutral reactions between CH_3 and atomic oxygen, where CH_3 is built from carbon ions reacting with molecular hydrogen (e.g., Wirström et al. 2012). Alternatively, formaldehyde is efficiently formed on the surface of icy dust grains via the hydrogenation of CO (e.g., Charnley et al. 1997; Watanabe & Kouchi 2002). Subsequently, it may be released into the gas phase by photoevaporation or shocks and then behave, in the first case, like a tracer of photon dominated regions (PDRs), and in the second like a shock tracer. The relative importance of the two main pathways of H_2CO formation, gas-phase chemistry or dust grain mantle evaporation, is poorly constrained.

Small differences in the zero point energy between reactants and products of isotopically distinct species may cause fractionation. Due to the charge exchange reaction of CO with $^{13}\text{C}^+$ (Watson et al. 1976), gas phase CO should have a tendency to be enriched in ^{13}C . Other molecules, like perhaps H_2CO , formed in the gas phase through different chemical pathways, should then be depleted in the ^{13}C bearing isotopologue (e.g., Langer et al. 1984). However, if most of the formaldehyde originates alternatively from dust grain mantles, the situation is different. In this case, H_2CO formed by the hydrogenation of CO, would be similarly enriched in ^{13}C as CO.

As a result, the carbon isotope ratios obtained from formaldehyde could be similar or larger than that from C^{18}O and could provide us with a useful hint for the predominant H_2CO formation scenario in massive star

forming regions. In previous studies (see, e.g., Milam et al. 2005), larger values were found, suggesting a predominantly gas-phase origin of formaldehyde. In this study, however, we find slightly smaller values, consistent with formaldehyde formation on dust grains and subsequent release into the interstellar medium. Within the range of uncertainty, it could even contradict both grain mantle and gas phase formation scenarios outlined above. First results from four sources, hinting at this latter possibility, i.e. suggesting significantly ^{13}C enhanced formaldehyde as compared to CO and methanol (CH_3OH), were already published by Wiström et al. 2012. Constructing more extensive fractionation networks including both gas-phase, dust grain and gas-dust interactions might provide further insight into this interesting and quite basic astrochemical puzzle.

5. SUMMARY

With the Tianma Radio Telescope (TMRT), we performed observations of the $1_{10} - 1_{11}$ and $2_{11} - 2_{12}$ lines of H_2CO and the $1_{10} - 1_{11}$ line of H_2^{13}CO toward a big sample of 112 Galactic molecular lines-of-sight. All three lines are detected toward 38 targets (43 radial velocity components), with a detection rate of $\sim 34\%$. For these 38 sources, their continuum at C- (~ 5 GHz) and Ku-band (14.5 GHz) were also observed and detected, at C-band in all sources and, at Ku-band, in 32 objects. Spectral line and continuum data for those 38 sources were analyzed. Our main results are :

1. Based on spectral line parameters and continuum temperatures, we obtained column densities, optical depths and the molecular abundance ratios.
2. We used the RADEX non-LTE model for the radiative transfer and took the new collision rates from Wiesenfeld & Faure (2013) to determine the photon trapping effect in the mm-wave lines connecting the $J = 1$ and 2 K-doublets of ortho- H_2CO .
3. We took reliable distance values from trigonometric parallax measurements and the Revised Kinematic Distance Calculator (Reid et al. 2014) for our sources. Thus the $^{12}\text{C}/^{13}\text{C}$ gradient along the Galactocentric distance is confirmed from a linear fit to the $^{12}\text{C}/^{13}\text{C}$ data resulting in $(5.08 \pm 1.10)D_{GC} + (11.86 \pm 6.60)$, with a correlation coefficient of 0.58. Measurements of more sources, especially those with large Galactocentric distance, are needed to further improve the statistical significance.
4. The gradient determined by us is flatter than that obtained from previous studies of formaldehyde, but is consistent, within the uncertainties, with those obtained from CN and C^{18}O . While the previous results may suggest an H_2CO formation mechanism dominated by gas-phase reactions, our new result tends to support a formation on dust grain mantles followed by evaporation.

This work is supported by the Natural Science Foundation of China (No. 11473007, 11590782) and the Guangzhou Education Bureau (No. 1201410593). We would like to thank for the assistance of the TMRT operators during the observations. Y.T.Y. wishes to thank J.Z.Wang and X.Chen for their help with the observations and comments.

Software: GILDAS/CLASS (Pety 2005, GILDAS team 2013), RADEX (Van der Tak et al. 2007)

REFERENCES

- | | |
|---|---|
| <p>Araya, E., Hofner, P., Churchwell, E., & Kurtz, S. 2002, ApJS, 138, 63</p> <p>Araya, E., Hofner, P., Goss, W. M., et al. 2007, ApJS, 170, 152</p> <p>Charnley, S. B., Tielens, A. G. G. M., & Rodgers, S. D. 1997, ApJ, 482, L203</p> <p>Chen X. et al. 2017, MNRAS, 466, 4364</p> <p>Choi, Y. K., Hachisuka, K., Reid, M. J., et al. 2014, ApJ, 790, 99</p> | <p>Dong, J., Fu, L., Liu, Q., et al. 2018, ExA, 45, 397</p> <p>Dong, J., Zhong, W., Wang, J., Liu, Q., et al. 2018, ITAP, 66, 2044.</p> <p>Evans, N. J. II, Zuckerman, B., Morris, G., Sato, T. 1975, ApJ, 196, 433</p> <p>Gardner, F. F., & Whiteoak, J. B. 1979, MNRAS, 188, 331</p> <p>Ginsburg, A., Darling, J., Battersby, C., Zeiger, B., & Bally, J. 2011, ApJ, 736, 149</p> |
|---|---|

Table 4. Comparison of $^{12}\text{C}/^{13}\text{C}$ ratios from H_2CO , CN, and CO

Source	D_{GC} (kpc)	H_2CO		CN^b	CO^c
		This paper	Previous results ^a		
W3IRS5	10.3	60 ± 11
Mol12	9.71	47 ± 8
NGC2024	7.22	52 ± 6	72 ± 11	65 ± 12	...
M-0.13	0.06	11.10 ± 0.08
Sgr A	0.17	10.71 ± 0.11
Sgr B2	7.81	77 ± 15
	0.38	11.48 ± 0.03	10	$\geq 18_{-6}$	24 ± 1
M+1.6	0.77	10.15 ± 0.68
G10.16-0.35	7.44	24 ± 4
	6.24	42 ± 3
W31	3.38	16 ± 4	37 ± 6	20 ± 6	...
	5.0	47 ± 5
G11.93-0.61	4.88	45 ± 7
W33	5.32	23 ± 1	74 ± 22	37 ± 8	$39 \pm 1, 43 \pm 4^d$
G13.88+0.28	4.41	35 ± 6
G12.91-0.26	5.69	49 ± 3
G19.62-0.23	5.23	28 ± 3	41 ± 4	71 ± 17	...
G023.44-00.18	2.48	18 ± 13
	3.59	30 ± 3
G23.43-0.21	3.9	39 ± 4
G29.9-0.0	4.38	44 ± 9	45 ± 5	63 ± 27	...
G31.41+0.31	4.51	32 ± 2
W43	4.58	26 ± 1	42 ± 6
G34.26+0.15	5.58	46 ± 4
G34.3+0.1	5.58	31 ± 4	58 ± 5	28 ± 4	...
J185648.26	4.8	48 ± 5
G37.76-0.20	5.62	34 ± 23
G35.20-1.74	5.77	43 ± 6
G35.2-1.8	6.16	53 ± 11	55 ± 5	64 ± 24	...
G043.16+00.01	7.6	39 ± 14
G43.17+0.00	7.56	40 ± 13
G43.2+0.0	7.55	72 ± 46	74 ± 20	44 ± 22	49 ± 6
G45.45+0.06	6.39	30 ± 4
G49.21-0.35	6.15	99 ± 24	58 ± 4	$\geq 33_{-13}$...
J192311.17	6.31	18 ± 9
	6.17	59 ± 4
G49.4-0.3	6.17	86 ± 7	81 ± 12
G49.5-0.4	6.18	45 ± 16	70 ± 11
J192345.73	6.18	19 ± 8
J203901.04	8.14	64 ± 7
DR21	8.05	48 ± 3	73 ± 11	36 ± 3	53 ± 2
J205658.56	7.38	42 ± 5
J205703.98	7.37	26 ± 8
W3-OH	9.58	...	91 ± 16	63 ± 6	$66 \pm 4, 85 \pm 15^d$
W51M	6.18	35 ± 12	45 ± 2
Orion A	8.49	43 ± 7	79 ± 7
Orion Bar	8.49	70 ± 11	75 ± 9^e
NGC7538	9.42	56 ± 10	56 ± 10
S156	10.34	78 ± 44	...
WB89 391	14.25	134 ± 43	...

^a From Henkel et al. (1980, 1982, 1983, 1985).^b From Milam et al. (2005), Savage et al. (2002).^c From Langer & Penzias (1990).^d From Wouterloot & Brand (1996).^e From Keene et al. (1998).

Table 5. Measurements of the $^{12}\text{C}/^{13}\text{C}$ gradient.

	Previous fitting results ^a		This work ^b	
	slope	intercept	slope	intercept
CN ^c	6.01 ± 1.19	12.28 ± 9.33	6.87 ± 1.46	5.06 ± 11.07
C ¹⁸ O ^d	5.41 ± 1.07	19.03 ± 7.90	5.90 ± 1.32	15.30 ± 9.65
H ₂ CO ^e	7.60 ± 1.79	18.05 ± 10.88	8.66 ± 1.64	9.30 ± 10.37
This work (H ₂ CO)	4.94 ± 0.96	9.37 ± 6.05	5.08 ± 1.10	11.86 ± 6.60

NOTE—The ^a and ^b represent the fitting results for the old and new distances, respectively. For this work, ^a and ^b also represent the corrected results using the collision rates of H₂CO taken from Green et al. (1991) and Wiesenfeld & Faure (2013), respectively.

^c From Milam et al. (2005).

^d From Langer & Penzias (1990), Wouterloot & Brand (1996) and Keene et al. (1998).

^e From Henkel et al. (1980, 1982, 1983, 1985).

- Gravity Collaboration, Abuter R., Amorim A., et al. 2018, A&A, 615, L15
- Green S. 1991, ApJS, 76, 979
- Güsten, R., Henkel, C., & Batrla, W. 1985, A&A, 149, 195
- Henkel, C., Güsten, R., Gardner, F. F. 1985, A&A, 143, 148
- Henkel, C., Walmsley, C. M., & Wilson, T. L. 1980, A&A, 82, 41
- Henkel, C., Wilson, T. L., & Pankonin, V. 1981, A&A, 99, 270
- Henkel, C., Wilson, T. L., & Bieging, J. 1982, A&A, 109, 344
- Henkel, C., Wilson, T. L., Walmsley, C. M., & Pauls, T. 1983, A&A, 127, 388
- Henkel, C., Wilson, T. L., Langer, N., Chin, Y.-N., & Mauersberger, R. 1994, in *The Structure and Content of Molecular Clouds*, eds. T. L. Wilson & K. J. Johnston (Berlin Springer: Verlag), LNP, 439, 72
- Johnson, D. R., Lovas, F. J., & Kirchhoff, W. H. 1972, JPCRD, 1, 1011
- Keene, J., Schilke, P., Kooi, J., Lis, D. C., Mehringer, D. & Phillips, T. G. 1998, ApJ, 494, L107
- Kukulich, S. G., & Rubin, D. J. 1971, JMoSp, 38, 130
- Langer, W. D., Graedel, T. E., & Armentrout, P. B. 1984, ApJ, 277, 581
- Langer, W. D., & Penzias, A. A. 1990, ApJ, 357, 477
- Li, J. et al. 2016, ApJ, 824, 136
- Mangum, J. G., Wootten, A., Loren, R. B., & Wadiak, E. J. 1990, ApJ, 348, 542
- Menten, K. M., Reid, M. J., Forbrich, J., & Brunthaler, A. 2007, A&A, 474, 515
- Meyer, B. S., 1994, ARA&A, 32, 153.
- Milam, S. N., Savage, C., Brewster, M. A., Ziurys, L. M., & Wyckoff, S. 2005, ApJ, 634, 1126
- Pilkington, K., Few, C. G., Gibson, B. K. et al. 2012, A&A, 5540, 56
- Perley, R. A., & Butler, B. J. 2013, ApJS, 204, 19
- Reid, M. J., Menten, K. M., Zheng, X. W., et al. 2009, ApJ, 700, 137
- Reid, M. J., Menten, K. M., Brunthaler, A., et al. 2014, ApJ, 783, 130
- Reifenstein, E. C., Wilson, T. L., Burke, B. F., Mezger, P. G., & Altenhoff, W. J. 1970, A&A, 4, 357
- Riquelme, D., Amo-Baladrón, M. A., & Martín-Pintado, J. et al. 2010, A&A, 523, A51
- Rivera-Ingraham, A., et al. 2010, ApJ, 723, 915
- Roman-Duval, J., Jackson, J. M., Heyer, M., et al. 2009, ApJ, 699, 1153
- Savage, C., Apponi, A. J., Ziurys, L. M., & Wyckoff, S. 2002, ApJ, 578, 211
- Sewilo, M., Watson, C., Araya, E., Churchwell, E., Hofner, P., & Kurtz, S. 2004, ApJS, 154, 553
- Tang, X. D., Henkel, C., Menten, K. M., et al. 2017a, A&A, 598, 30
- Troscnpt N., Faure A., Wiesenfeld L., Ceccarelli C., Valiron P. 2009a, A&A, 493, 687
- Troscnpt N., Faure A., Maret S., Ceccarelli C., Hily-Blant P., Wiesenfeld L. 2009b, A&A, 506, 1243
- Tucker, K. D., Tomasevich, G. R., Thaddeus, P. 1971, ApJ, 169, 429
- Van der Tak, F.F.S., Black, J.H., Schier, F.L., Jansen, D.J., van Dishoeck, E.F. 2007, A&A, 468, 627-635
- Wang, M., Henkel, C., Chin, Y.-N., Whiteoak, J. B., Hunt Cunningham, M., Mauersberger, R., & Muders, D. 2004, A&A, 422, 883
- Watanabe, N., & Kouchi, A. 2002, ApJ, 571, L173
- Watson, W. D., Anicich, V. G., & Huntress, W. T. Jr. 1976, ApJ, 205, L165
- Watson, C., Araya, E., Sewilo, M., Churchwell, E., Hofner, P., & Kurtz, S. 2003, ApJ, 587, 714
- Wiesenfeld, L., & Faure, A. 2013, MNRAS, 432, 2573
- Wilson, T. L., Bieging, J., Downes, D., Gardner, F. F. 1976, A&A, 51, 303
- Wilson, T. L. & Rood, R. T. 1994, ARA&A, 32, 191
- Wirstrom, E. S., Charnley, S. B., Geppert, W. D., & Persson, C. M. 2012, LPSC, 43, 1611
- Wouterloot, J. G. A., & Brand, J. 1996, A&AS, 119, 439
- Zapata, L. A., Ho, P. T. P., Schilke, P., et al. 2009, ApJ, 698, 1422
- Zuckerman, B., Buhl, D., Palmer, P., & Snyder, L. E. 1974, ApJ, 189, 217

APPENDIX

A.

Table 6. H_2^{12}CO and H_2^{13}CO $1_{10} - 1_{11}$ observations of the entire sample

Sources	R.A.(J2000) (h m s)	Dec.(J2000) (° ' ")	Line	Integration time (minutes)	rms (mK)	ΔV (km s ⁻¹)
(1)	(2)	(3)	(4)	(5)	(6)	(7)
G121.29+00.65 ^a	00:36:47.35	63:29:02.2	H_2^{12}CO (C)	90	11.1	0.089
			H_2^{13}CO (C)	82	10.8	0.093
IRAS00338 ^a	00:36:47.50	63:29:02.0	H_2^{12}CO (C)	39	17.0	0.089
			H_2^{13}CO (C)	39	17.8	0.093
G122.01-07.08 ^a	00:44:58.40	55:46:47.6	H_2^{12}CO (C)	90	11.4	0.089
			H_2^{13}CO (C)	90	11.0	0.093
G123.06-06.30 ^a	00:52:24.20	56:33:43.2	H_2^{12}CO (C)	30	19.4	0.089
			H_2^{13}CO (C)	30	20.6	0.093
G134.62-02.19 ^b	02:22:51.71	58:35:11.4	H_2^{12}CO (C)	42	15.3	0.089
			H_2^{13}CO (C)	42	15.3	0.093
W3IRS5	02:25:40.80	62:05:53.00	H_2^{12}CO (C)	42.9	48.2	0.178
			H_2^{13}CO (C)	102	15.2	0.374
			H_2^{12}CO (Ku)	40	67.4	0.059
W3 ^a	02:25:44.19	62:06:00.9	H_2^{12}CO (C)	276	17.2	0.089
			H_2^{13}CO (C)	438	19.1	0.093
W3-OH ^a	02:27:03.82	61:52:25.2	H_2^{12}CO (C)	88	12.2	0.089
			H_2^{13}CO (C)	88	12.3	0.093
G133.947 ^a	02:27:16.50	61:52:24.5	H_2^{12}CO (C)	60	18.8	0.089
			H_2^{13}CO (C)	42.9	20.1	0.093
G135.27+02.79 ^b	02:43:28.57	62:57:08.4	H_2^{12}CO (C)	30	23.6	0.089
			H_2^{13}CO (C)	30	23.6	0.093
WB443 ^b	02:47:15.43	60:30:49.0	H_2^{12}CO (C)	30	20.9	0.089
			H_2^{13}CO (C)	30	20.9	0.093
WB448 ^b	02:50:08.6	61:59:52.3	H_2^{12}CO (C)	30	24.4	0.089
			H_2^{13}CO (C)	30	24.4	0.093
G138.295 ^b	03:00:10.08	02:12:09.1	H_2^{12}CO (C)	39	22.2	0.089
			H_2^{13}CO (C)	39	22.2	0.093
AFGL490 ^a	03:27:38.80	58:47:00.0	H_2^{12}CO (C)	42.9	17.6	0.089
			H_2^{13}CO (C)	42.9	35.2	0.093
G160.14+03.15 ^b	05:01:40.24	47:07:19.0	H_2^{12}CO (C)	28	23.0	0.089
			H_2^{13}CO (C)	28	23.0	0.093
G168.06+00.82 ^b	05:17:13.74	39:22:19.9	H_2^{12}CO (C)	28	21.4	0.089
			H_2^{13}CO (C)	28	21.4	0.093
ORI ^b	05:35:17.46	-05:23 15.7	H_2^{12}CO (C)	39	128	0.089
			H_2^{13}CO (C)	39	128	0.093
G176.51+00.20 ^a	05:37:52.14	32:00:03.9	H_2^{12}CO (C)	30	19.6	0.089
			H_2^{13}CO (C)	30	18.9	0.093
IRAS05358 ^a	05:39:13.00	35:45:49.0	H_2^{12}CO (C)	42.9	15.3	0.089
			H_2^{13}CO (C)	42.9	15.2	0.093
G182.67-03.26 ^b	05:39:28.42	24:56:32.1	H_2^{12}CO (C)	30	19.9	0.089
			H_2^{13}CO (C)	30	19.9	0.093

Table 6 continued on next page

Table 6 (continued)

Sources	R.A.(J2000)	Dec.(J2000)	Line	Integration time	rms	ΔV
	(h m s)	($^{\circ}$ ' ")		(minutes)	(mK)	(km s $^{-1}$)
(1)	(2)	(3)	(4)	(5)	(6)	(7)
G183.72-03.66 ^a	05:40:24.23	23:50:54.7	H ₂ ¹² CO (C)	20	24.6	0.089
			H ₂ ¹³ CO (C)	20	21.2	0.093
Mol12	05:40:24.40	23:50:54	H ₂ ¹² CO (C)	432	5.5	0.089
			H ₂ ¹³ CO (C)	402	4.3	0.093
			H ₂ ¹² CO (Ku)	40	31.5	0.059
NGC2024	05:41:45.50	-01:54:46.7	H ₂ ¹² CO (C)	120	23.1	0.089
			H ₂ ¹³ CO (C)	102	15.1	0.187
			H ₂ ¹² CO (Ku)	40	43.5	0.059
G192.16-03.81 ^a	05:58:13.53	16:31:58.9	H ₂ ¹² CO (C)	28	14.6	0.178
			H ₂ ¹³ CO (C)	28	20.3	0.093
MonR2 ^b	06:07:52.43	-01:06:50.8	H ₂ ¹² CO (C)	29.2	19.4	0.089
			H ₂ ¹³ CO (C)	29.2	19.4	0.093
G188.94+00.88 ^a	06:08:53.35	21:38:28.7	H ₂ ¹² CO (C)	28	20.1	0.089
			H ₂ ¹³ CO (C)	28	18.5	0.093
G188.79+01.03 ^a	06:09:06.97	21:50:41.4	H ₂ ¹² CO (C)	30	16.5	0.089
			H ₂ ¹³ CO (C)	30	17.8	0.093
H192.584 ^b	06:10:56.51	-01:06:53.3	H ₂ ¹² CO (C)	39	21.9	0.089
			H ₂ ¹³ CO (C)	39	21.9	0.093
G192.60-00.04 ^a	06:12:54.02	17:59:23.3	H ₂ ¹² CO (C)	38	16.3	0.089
			H ₂ ¹³ CO (C)	38	18.2	0.093
G196.45-01.67 ^a	06:14:37.08	13:49:36.7	H ₂ ¹² CO (C)	60	14.4	0.089
			H ₂ ¹³ CO (C)	60	15.2	0.093
NGC2264-1 ^a	06:41:09.80	09:29:32.0	H ₂ ¹² CO (C)	39	18.5	0.089
			H ₂ ¹³ CO (C)	39	16.9	0.093
G211.59+01.05 ^b	06:52:45.32	01:40:23.1	H ₂ ¹² CO (C)	38	17.9	0.089
			H ₂ ¹³ CO (C)	38	17.9	0.093
G239.35-05.06 ^b	07:22:58.33	-25:46:03.1	H ₂ ¹² CO (C)	34	17.1	0.089
			H ₂ ¹³ CO (C)	34	17.1	0.093
G229.57+00.15 ^a	07:23:01.84	-14:41:32.8	H ₂ ¹² CO (C)	60	11.6	0.089
			H ₂ ¹³ CO (C)	60	13.8	0.093
G232.62+00.99 ^a	07:32:09.78	-16:58:12.8	H ₂ ¹² CO (C)	82	12.5	0.089
			H ₂ ¹³ CO (C)	108	10.5	0.093
G236.81+01.98 ^a	07:44:28.24	-20:08:30.2	H ₂ ¹² CO (C)	28	19.8	0.089
			H ₂ ¹³ CO (C)	28	18.5	0.093
G240.31+00.07 ^b	07:44:51.92	-24:07:41.5	H ₂ ¹² CO (C)	28	20.5	0.089
			H ₂ ¹³ CO (C)	28	20.5	0.093
IRC+10216 ^b	09:47:57.49	13:16:47.8	H ₂ ¹² CO (C)	102	11.2	0.089
			H ₂ ¹³ CO (C)	102	11.2	0.093
M-0.13	17:45:37.37	-29:05:19.74	H ₂ ¹² CO (C)	33.2	41.2	0.089
			H ₂ ¹³ CO (C)	39	16.5	0.84
			H ₂ ¹² CO (Ku)	8	42.5	0.059
Sgr A	17:45:42.63	-29:00:32.39	H ₂ ¹² CO (C)	24	99.2	0.089
			H ₂ ¹³ CO (C)	24	39.6	0.747
			H ₂ ¹² CO (Ku)	16	78.5	0.059
Sgr B2	17:47:20.00	-28:22:40.0	H ₂ ¹² CO (C)	32	186	0.178
			H ₂ ¹³ CO (C)	32	24.1	0.093

Table 6 continued on next page

Table 6 (*continued*)

Sources	R.A.(J2000)	Dec.(J2000)	Line	Integration time	rms	ΔV
	(h m s)	($^{\circ}$ ' ")		(minutes)	(mK)	(km s $^{-1}$)
(1)	(2)	(3)	(4)	(5)	(6)	(7)
M+1.6	17:49:22.90	-27:34:02.11	H ₂ ¹² CO (Ku)	36	65.6	0.059
			H ₂ ¹² CO (C)	39	23.0	0.089
			H ₂ ¹³ CO (C)	39	9.9	0.467
G19.6-0.2	18 27:38.05	-11:56:41.4	H ₂ ¹² CO (Ku)	8	42.3	0.059
			H ₂ ¹² CO (C)	27.3	24.0	0.089
			H ₂ ¹³ CO (C)	39	24.3	0.093
G005.88-00.39 ^a	18:00:30.31	-24:04:04.5	H ₂ ¹² CO (C)	28	15.2	0.178
			H ₂ ¹³ CO (C)	28	15.4	0.093
G009.62+00.19 ^a	18:06:14.66	-20:31:31.7	H ₂ ¹² CO (C)	22	16.3	0.178
			H ₂ ¹³ CO (C)	22	25.8	0.093
G010.47+00.02 ^a	18:08:38.23	-19:51:50.3	H ₂ ¹² CO (C)	66	12.5	0.089
			H ₂ ¹³ CO (C)	66	14.8	0.093
G10.16-0.35	18:09:24.60	-20:19:29.0	H ₂ ¹² CO (C)	180	8.5	0.178
			H ₂ ¹³ CO (C)	180	7.7	0.187
			H ₂ ¹² CO (Ku)	8	48.2	0.059
W31	18:10:28.55	-19:55:48.6	H ₂ ¹² CO (C)	114	16.7	0.178
			H ₂ ¹³ CO (C)	108	6.3	0.374
			H ₂ ¹² CO (Ku)	8	42.6	0.059
G011.91-00.61 ^a	18:13:58.12	-18:54:20.3	H ₂ ¹² CO (C)	28	21.8	0.089
			H ₂ ¹³ CO (C)	28	20.0	0.093
G11.93-0.61	18:14:01.00	-18:53:23.0	H ₂ ¹² CO (C)	80	13.7	0.089
			H ₂ ¹³ CO (C)	80	9.5	0.187
			H ₂ ¹² CO (Ku)	8	41.0	0.059
W33	18:14:13.98	-17:55:50.17	H ₂ ¹² CO (C)	30	34.3	0.089
			H ₂ ¹³ CO (C)	60	26.1	0.093
			H ₂ ¹² CO (Ku)	20	68.9	0.059
G13.88+0.28	18:14:35.20	-16:45:21.0	H ₂ ¹² CO (C)	80	15.3	0.089
			H ₂ ¹³ CO (C)	76	12.7	0.093
			H ₂ ¹² CO (Ku)	8	37.7	0.059
G12.91-0.26	18:14:39.00	-17:52:03.0	H ₂ ¹² CO (C)	78	15.1	0.089
			H ₂ ¹³ CO (C)	80	10.5	0.093
			H ₂ ¹² CO (Ku)	8	37.9	0.059
G011.49-01.48 ^a	18:16:22.13	-19:41:27.2	H ₂ ¹² CO (C)	28	15.3	0.178
			H ₂ ¹³ CO (C)	28	19.8	0.093
M17 ^a	18:20:26.14	-16.11.24.0	H ₂ ¹² CO (C)	96	49.6	0.089
			H ₂ ¹³ CO (C)	180	55.4	0.093
J182708.27 ^b	18:27:08.27	-10.46.09.9	H ₂ ¹² CO (C)	60	14.4	0.089
			H ₂ ¹³ CO (C)	60	14.4	0.093
G19.62-0.23	18:27:38.08	-11:56:35.5	H ₂ ¹² CO (C)	132	9.9	0.178
			H ₂ ¹³ CO (C)	132	8.9	0.187
			H ₂ ¹² CO (Ku)	8	41.5	0.059
G023.44-00.18	18:34:39.19	-08:31:25.4	H ₂ ¹² CO (C)	198	8.2	0.178
			H ₂ ¹³ CO (C)	210	8.0	0.374
			H ₂ ¹² CO (Ku)	8	48.8	0.059
G23.43-0.21	18:34:43.60	-08:32:25.0	H ₂ ¹² CO (C)	138	6.3	0.355
			H ₂ ¹³ CO (C)	132	5.7	0.374

Table 6 continued on next page

Table 6 (*continued*)

Sources	R.A.(J2000)	Dec.(J2000)	Line	Integration time	rms	ΔV
	(h m s)	($^{\circ}$ ' ")		(minutes)	(mK)	(km s $^{-1}$)
(1)	(2)	(3)	(4)	(5)	(6)	(7)
			H ₂ ¹² CO (Ku)	16	15.8	0.059
G029.95-00.01 ^a	18:46:03.74	-02:39:22.3	H ₂ ¹² CO (C)	26	15.7	0.178
			H ₂ ¹³ CO (C)	2	30.1	0.093
G29.9-0.0	18:46:08.10	-02:41:40.20	H ₂ ¹² CO (C)	120	7.8	0.178
			H ₂ ¹³ CO (C)	132	6.1	0.374
			H ₂ ¹² CO (Ku)	8	38.4	0.059
G31.41+0.31	18:47:34.60	-01:12:43.0	H ₂ ¹² CO (C)	72	13.4	0.089
			H ₂ ¹³ CO (C)	72	9.1	0.188
			H ₂ ¹² CO (Ku)	8	38.3	0.059
W43	18:47:36.68	-01:59:01.85	H ₂ ¹² CO (C)	30	29.2	0.089
			H ₂ ¹³ CO (C)	60	24.8	0.093
			H ₂ ¹² CO (Ku)	8	38.9	0.059
J184741.61 ^a	18:47:41.61	-01:35:05.3	H ₂ ¹² CO (C)	56	8.4	0.089
			H ₂ ¹³ CO (C)	56	14.8	0.093
J184754.69 ^a	18:47:54.70	-01:34:57.0	H ₂ ¹² CO (C)	60	11.7	0.178
			H ₂ ¹³ CO (C)	60	16.2	0.093
G031.28+00.06 ^a	18:48:12.39	-01:26:30.7	H ₂ ¹² CO (C)	62	9.3	0.178
			H ₂ ¹³ CO (C)	62	13.7	0.093
G34.26+0.15	18:53:18.54	01:14:58	H ₂ ¹² CO (C)	80	15.1	0.089
			H ₂ ¹³ CO (C)	80	12.6	0.188
			H ₂ ¹² CO (Ku)	8	42.8	0.059
J185319.73 ^b	18:53:19.73	00:29:59.8	H ₂ ¹² CO (C)	30	19.6	0.089
			H ₂ ¹³ CO (C)	30	19.6	0.093
G34.3+0.1	18:53:20.21	01:14:31.74	H ₂ ¹² CO (C)	33.2	19.2	0.178
			H ₂ ¹³ CO (C)	39	22.1	0.093
			H ₂ ¹² CO (Ku)	8	46.0	0.059
J185648.26	18:56:48.27	01:18:47	H ₂ ¹² CO (C)	72	16.3	0.089
			H ₂ ¹³ CO (C)	102	9.6	0.187
			H ₂ ¹² CO (Ku)	8	35.3	0.059
G37.76-0.20	19:00:59.30	04:12:06	H ₂ ¹² CO (C)	120	9.8	0.089
			H ₂ ¹³ CO (C)	120	7.7	0.187
			H ₂ ¹² CO (Ku)	16	28.2	0.059
G35.20-1.74	19:01:47.00	01:13:08	H ₂ ¹² CO (C)	186	18.2	0.089
			H ₂ ¹³ CO (C)	186	9.1	0.187
			H ₂ ¹² CO (Ku)	8	45.2	0.059
G35.2-1.8	19:01:47.76	01:12:51	H ₂ ¹² CO (C)	79.1	17.0	0.178
			H ₂ ¹³ CO (C)	83	9.5	0.187
			H ₂ ¹² CO (Ku)	20	38.7	0.059
G49.2-0.3 ^a	19:23:01.21	14:16:40.4	H ₂ ¹² CO (C)	60	21.4	0.089
			H ₂ ¹³ CO (C)	60	26.8	0.093
G043.16+00.01	19:10:13.41	09:06:12.8	H ₂ ¹² CO (C)	26	45.4	0.355
			H ₂ ¹³ CO (C)	26	20.4	0.374
			H ₂ ¹² CO (Ku)	4	129	0.059
G43.17+0.00	19:10:15.30	09:06:17	H ₂ ¹² CO (C)	150	16.0	0.089
			H ₂ ¹³ CO (C)	150	12.5	0.187
			H ₂ ¹² CO (Ku)	8	55.7	0.059

Table 6 continued on next page

Table 6 (*continued*)

Sources	R.A.(J2000)	Dec.(J2000)	Line	Integration time	rms	ΔV
	(h m s)	($^{\circ}$ ' ")		(minutes)	(mK)	(km s $^{-1}$)
(1)	(2)	(3)	(4)	(5)	(6)	(7)
G43.2+0.0	19:10:15.71	09:06:05.48	H ₂ ¹² CO (C)	39	64.5	0.178
			H ₂ ¹³ CO (C)	39	18.7	0.374
			H ₂ ¹² CO (Ku)	12	57.3	0.059
W49 ^a	19:10:17.61	09:05:58.6	H ₂ ¹² CO (C)	30	35.5	0.089
			H ₂ ¹³ CO (C)	60	25.9	0.093
G043.79-00.12 ^a	19:11:53.99	09:35:50.3	H ₂ ¹² CO (C)	26	14.9	0.178
			H ₂ ¹³ CO (C)	26	21.6	0.093
G045.07+00.13 ^b	19:13:22.04	10:50:53.3	H ₂ ¹² CO (C)	18	23.5	0.089
			H ₂ ¹³ CO (C)	18	23.5	0.093
G45.45+0.06	19:14:21.30	11:09:13	H ₂ ¹² CO (C)	132	13.3	0.089
			H ₂ ¹³ CO (C)	138	10.5	0.093
			H ₂ ¹² CO (Ku)	4	25.3	0.059
G043.89-00.78 ^a	19:14:26.39	09:22:36.5	H ₂ ¹² CO (C)	58	14.8	0.089
			H ₂ ¹³ CO (C)	58	13.7	0.093
G49.21-0.35	19:23:02.10	14:16:40	H ₂ ¹² CO (C)	120	14.5	0.089
			H ₂ ¹³ CO (C)	120	15.8	0.093
			H ₂ ¹² CO (Ku)	16	39.9	0.059
J192311.17	19:23:11.17	14:26:33	H ₂ ¹² CO (C)	132	10.7	0.089
			H ₂ ¹³ CO (C)	138	10.5	0.187
			H ₂ ¹² CO (Ku)	8	40.1	0.059
G49.4-0.3	19:23:14.01	14:27:07	H ₂ ¹² CO (C)	84	21.8	0.089
			H ₂ ¹³ CO (C)	108	12.2	0.187
			H ₂ ¹² CO (Ku)	8	38.2	0.059
G052.10+01.04 ^b	19:23:37.32	17:29:10.5	H ₂ ¹² CO (C)	16	34.1	0.089
			H ₂ ¹³ CO (C)	16	34.1	0.093
G49.5-0.4	19:23:43.96	14:30:33	H ₂ ¹² CO (C)	40	41.1	0.089
			H ₂ ¹³ CO (C)	40	37.2	0.187
			H ₂ ¹² CO (Ku)	8	54.4	0.059
J192345.73	19:23:45.74	14:28:45	H ₂ ¹² CO (C)	78	18.3	0.178
			H ₂ ¹³ CO (C)	114	23.3	0.187
			H ₂ ¹² CO (Ku)	4	63.5	0.059
G61.48+0.09 ^a	19:46:47.33	25:12:45.6	H ₂ ¹² CO (C)	10	26.9	0.178
			H ₂ ¹³ CO (C)	20	51.3	0.093
G70.33+1.59 ^a	20:01:54.50	33:34:15.0	H ₂ ¹² CO (C)	60	17.5	0.089
			H ₂ ¹³ CO (C)	60	19.7	0.093
G069.54-00.97 ^a	20:10:09.07	31:31:36.0	H ₂ ¹² CO (C)	28	23.1	0.089
			H ₂ ¹³ CO (C)	28	17.7	0.093
G075.29+01.32 ^b	20:16:16.01	37:35:45.8	H ₂ ¹² CO (C)	12	36.8	0.089
			H ₂ ¹³ CO (C)	12	36.8	0.093
G074.03-01.71 ^a	20:25:07.11	34:49:57.6	H ₂ ¹² CO (C)	78	10.3	0.089
			H ₂ ¹³ CO (C)	88	12.0	0.093
G079.87+01.17 ^b	20:30:29.14	41:15:53.6	H ₂ ¹² CO (C)	46	14.7	0.089
			H ₂ ¹³ CO (C)	46	14.7	0.093
W75N ^a	20:38:36.93	42:37:37.5	H ₂ ¹² CO (C)	3	48.5	0.178
			H ₂ ¹³ CO (C)	5.9	51.6	0.093
J203901.04	20:39:01.00	42:19:53.0	H ₂ ¹² CO (C)	52	21.6	0.089

Table 6 continued on next page

Table 6 (*continued*)

Sources	R.A.(J2000)	Dec.(J2000)	Line	Integration time	rms	ΔV
	(h m s)	($^{\circ}$ ' ")		(minutes)	(mK)	(km s $^{-1}$)
(1)	(2)	(3)	(4)	(5)	(6)	(7)
			H ₂ ¹³ CO (C)	58	33.2	0.093
			H ₂ ¹² CO (Ku)	8	62.3	0.059
DR21	20:39:01.30	42:19:32.86	H ₂ ¹² CO (C)	108	17.8	0.089
			H ₂ ¹³ CO (C)	108	22.2	0.093
			H ₂ ¹² CO (Ku)	8	64.9	0.059
J205658.56	20:56:58.57	43:43:10.0	H ₂ ¹² CO (C)	64	15.4	0.089
			H ₂ ¹³ CO (C)	144	9.3	0.187
			H ₂ ¹² CO (Ku)	4	46.9	0.059
J205703.98	20:57:03.98	43:37:46.5	H ₂ ¹² CO (C)	102	14.0	0.089
			H ₂ ¹³ CO (C)	174	12.0	0.093
			H ₂ ¹² CO (Ku)	8	31.5	0.059
WB018 ^b	20:58:23.00	48:32:48.0	H ₂ ¹² CO (C)	52	18.2	0.089
			H ₂ ¹³ CO (C)	52	18.2	0.093
WB021 ^b	21:01:34.94	48:55:01.0	H ₂ ¹² CO (C)	30	18.6	0.089
			H ₂ ¹³ CO (C)	30	18.6	0.093
WB024 ^b	21:02:21.79	50:48:34.6	H ₂ ¹² CO (C)	28	24.0	0.089
			H ₂ ¹³ CO (C)	28	24.0	0.093
WB026 ^a	21:02:48.50	59:30:48.0	H ₂ ¹² CO (C)	64	13.6	0.089
			H ₂ ¹³ CO (C)	64	15.7	0.093
WB082 ^b	21:27:33.00	56:05:09.0	H ₂ ¹² CO (C)	30	19.2	0.089
			H ₂ ¹³ CO (C)	30	19.2	0.093
WB091 ^a	21:32:10.39	55:52:42.3	H ₂ ¹² CO (C)	28	15.7	0.178
			H ₂ ¹³ CO (C)	28	20.5	0.093
G105.41+09.8 ^a	21:43:06.48	66:06:55.3	H ₂ ¹² CO (C)	52	13.6	0.089
			H ₂ ¹³ CO (C)	56	16.2	0.093
WB140 ^b	21:56:15.09	57:50:41.9	H ₂ ¹² CO (C)	28	24.3	0.089
			H ₂ ¹³ CO (C)	28	24.3	0.093
WB160 ^b	22:15:09.51	58:49:06.0	H ₂ ¹² CO (C)	34	18.7	0.089
			H ₂ ¹³ CO (C)	34	18.7	0.093
G100.37-03.57 ^b	22:16:10.37	52:21:34.1	H ₂ ¹² CO (C)	44	15.6	0.089
			H ₂ ¹³ CO (C)	44	15.6	0.093
G107.29+05.63 ^b	22:21:26.73	63:51:37.9	H ₂ ¹² CO (C)	20	26.4	0.089
			H ₂ ¹³ CO (C)	20	26.4	0.093
CASA ^a	23.23:02.61	58:48:46.1	H ₂ ¹² CO (C)	108	103	0.089
			H ₂ ¹³ CO (C)	126	97.7	0.093
NGC7538 ^a	23:13:45.40	61:28:15.0	H ₂ ¹² CO (C)	126	12.6	0.089
			H ₂ ¹³ CO (C)	132	12.7	0.093

^a The sources only detected in the $1_{10} - 1_{11}$ lines of H₂¹²CO.

^b The sources not detected in both the $1_{10} - 1_{11}$ lines of H₂¹²CO and H₂¹³CO.

NOTE—Column (1): source name; Columns (2) and (3): Equatorial coordinates of sources; Column (4): molecular species, (C) and (Ku) indicate the C- and Ku-band, respectively; Column (5): integration time (ON-source + OFF-source); Column (6): rms noise obtained from Gaussian-fitting; Column (7): corresponding channel width.

B.

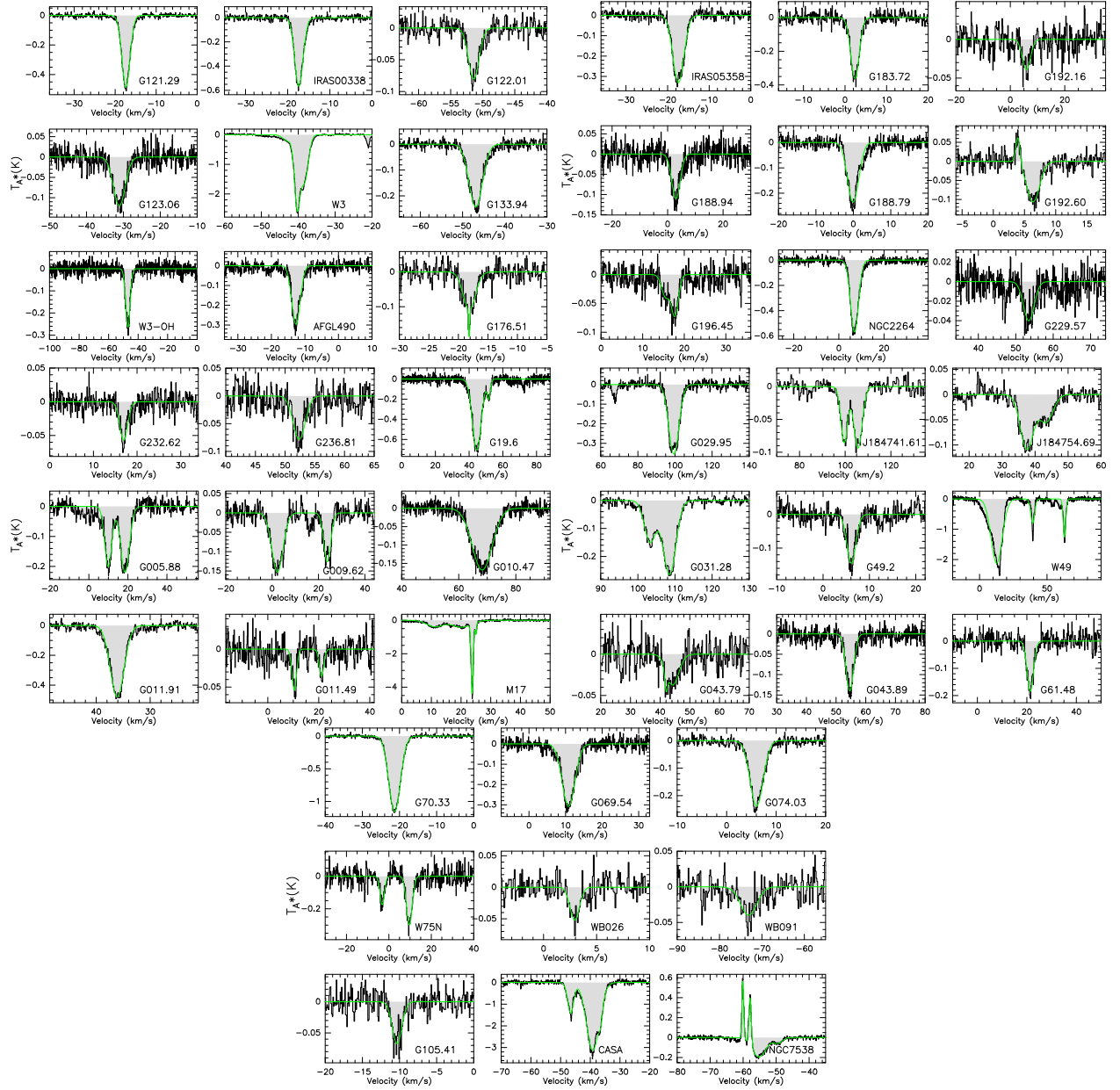


Figure 8. Spectra of 46 sources, only detected in the $1_0 - 1_1$ lines of H_2^{12}CO , after subtracting baselines and applying Hanning smoothing. Antenna temperature scales can be found on the left side of the profiles.

C.

Table 7. Gaussian-fitting results for 46 sources with only the $\text{H}_2^{12}\text{CO } 1_{10} - 1_{11}$ line detected

Source	$\int T_{mb} dv$	Velocity	Width	T _{peak}
(1)	(K km s ⁻¹) (2)	(km s ⁻¹) (3)	(km s ⁻¹) (4)	(K) (5)
G121.29+00.65	-1.217(0.008)	-17.357(0.007)	2.356(0.018)	-0.485
IRAS00338	-1.429(0.012)	-17.338(0.010)	2.366(0.024)	-0.567
G122.01-07.08	-0.168(0.007)	-51.397(0.041)	1.978(0.107)	-0.080
G123.06-06.30	-0.485(0.017)	-31.090(0.065)	3.814(0.155)	-0.119
W3	-4.627(0.331)	-40.345(0.042)	1.982(0.068)	-2.193
	-4.081(0.331)	-38.307(0.093)	2.55(0.142)	-1.504
G133.94+01.06	-0.991(0.012)	-46.865(0.022)	2.832(0.055)	-0.243
W3-OH	-0.984(0.035)	-46.049(0.055)	3.242(0.146)	-0.286
G133.947	-1.009(0.017)	-46.882(0.029)	3.586(0.188)	-0.264
AFGL490	-0.894(0.016)	-12.676(0.025)	2.874(0.064)	-0.292
G176.51+00.20	-0.302(0.014)	-18.141(0.051)	2.231(0.125)	-0.127
IRAS05358	-1.124(0.013)	-17.393(0.018)	3.178(0.040)	-0.332
G183.72-03.66	-0.943(0.018)	2.403(0.022)	2.448(0.056)	-0.362
G192.16-03.81	-0.157(0.016)	5.938(0.186)	3.667(0.445)	-0.040
G188.94+00.88	-0.385(0.019)	2.967(0.078)	3.324(0.205)	-0.109
G188.79+01.03	-0.888(0.016)	-0.052(0.032)	3.559(0.084)	-0.234
G192.60-00.04	-0.274(0.013)	6.464(0.054)	2.239(0.112)	-0.115
G196.45-01.67	-0.211(0.012)	17.158(0.092)	3.230(0.206)	-0.061
NGC2264-1	-2.538(0.017)	6.928(0.013)	4.189(0.032)	-0.569
G229.57+00.15	-0.143(0.010)	53.488(0.120)	3.362(0.291)	-0.040
G232.62+00.99	-0.145(0.009)	16.957(0.070)	2.365(0.202)	-0.058
G236.81+01.98	-0.183(0.015)	52.339(0.079)	2.190(0.247)	-0.078
G19.6-0.2	-4.689(0.037)	44.56(0.023)	6.231(0.061)	-0.707
	-0.452(0.023)	51.692(0.054)	2.285(0.089)	-0.186
G005.88-00.39	-0.924(0.031)	9.936(0.064)	4.327(0.193)	-0.201
	-1.244(0.031)	18.521(0.064)	5.332(0.149)	-0.219
G009.62+00.19	-0.935(0.028)	2.274(0.088)	5.736(0.189)	-0.153
	-0.484(0.022)	23.783(0.084)	3.587(0.179)	0.127
G010.47+00.02	-1.563(0.019)	68.161(0.052)	8.586(0.120)	-0.171
G011.91-00.61	-1.552(0.018)	36.113(0.017)	3.061(0.043)	-0.476
G011.49-01.48	-0.122(0.015)	10.389(0.132)	2.121(0.358)	-0.054
M17	-2.822(0.047)	11.977(0.089)	7.259(0.089)	-0.365

Table 7 continued on next page

Table 7 (*continued*)

Source	$\int T_{mb} dv$	Velocity	Width	T _{peak}
(1)	(K km s ⁻¹) (2)	(km s ⁻¹) (3)	(km s ⁻¹) (4)	(K) (5)
	-3.493(0.047)	21.342(0.089)	7.499(0.089)	-0.438
	-4.066(0.047)	23.768(0.089)	0.876(0.089)	-4.360
	-0.476(0.050)	25.031(0.089)	0.592(0.089)	-0.755
G029.95-00.01	-2.50(0.025)	99.403(0.044)	6.571(0.075)	-0.357
J184741.61	-0.318(0.016)	99.584(0.086)	3.512(0.214)	-0.085
	-0.435(0.017)	105.64(0.082)	4.368(0.202)	-0.094
J184754.69	-0.542(0.037)	37.541(0.149)	4.699(0.293)	-0.108
	-0.283(0.037)	43.377(0.33)	4.914(0.633)	-0.054
G031.28+00.06	-0.576(0.022)	103.317(0.058)	3.657(0.162)	-0.148
	-1.138(0.021)	108.533(0.036)	4.051(0.089)	-0.264
G49.2-0.3	-0.354(0.015)	6.098(0.047)	2.298(0.123)	-0.145
W49	-22.935(0.139)	12.668(0.028)	10.132(0.077)	-2.127
	-2.449(0.064)	39.470(0.023)	1.956(0.064)	-1.176
	-2.957(0.067)	62.935(0.022)	2.115(0.065)	-1.314
G043.79-00.12	-0.222(0.022)	43.776(0.259)	5.112(0.540)	-0.041
G043.89-00.78	-0.462(0.012)	54.643(0.036)	3.097(0.090)	-0.140
G61.48+0.09	-0.622(0.034)	21.406(0.084)	3.151(0.209)	-0.185
G70.33+1.59	-4.557(0.015)	-21.306(0.006)	3.714(0.014)	-1.153
G069.54-00.97	-1.360(0.021)	10.824(0.029)	4.153(0.078)	-0.308
G074.03-01.71	-0.787(0.010)	6.068(0.018)	3.125(0.045)	-0.237
W75N	-0.443(0.052)	-3.143(0.128)	2.372(0.354)	-0.175
	-1.033(0.057)	9.627(0.088)	3.251(0.211)	-0.298
WB026	-0.068(0.009)	2.952(0.072)	1.207(0.214)	-0.053
WB091	-0.161(0.021)	-73.164(0.220)	3.766(0.689)	-0.040
G105.41+09.8	-0.115(0.009)	-10.322(0.061)	1.575(0.137)	-0.068
CASA	-3.656(0.058)	-46.597(0.011)	2.441(0.049)	-1.407
	-16.523(0.169)	-39.265(0.023)	4.971(0.057)	-3.122
	-1.335(0.12)	-36.377(0.025)	1.591(0.083)	-0.788
NGC7538	-1.253(0.034)	-55.518(0.064)	6.289(0.192)	-0.187
	-0.123(0.011)	-49.113(0.085)	2.189(0.191)	-0.053

NOTE—Column (1): source name; Columns (2), (3), (4) and (5): the area, position, width and peak antenna temperature of Gaussian-fitting results respectively.